FULL FIELD STRAIN MEASUREMENT IN WELDS

By

Franklin Thompson Duvall
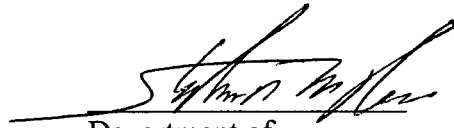
Bachelor of Science
Tennessee Technological University, 1990

Submitted in Partial Fulfillment of the

Requirements for the Degree of Master of Science

in the Department of Mechanical Engineering

College of Engineering
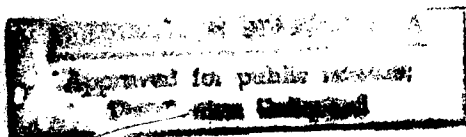
University of South Carolina

1998

Department of
Mechanical Engineering
Director of Thesis

Department of
Mechanical Engineering
2nd Reader

Dean of the Graduate School

ACKNOWLEDGMENTS

ABSTRACT

The intent of this study is to examine the stress-strain response of small material subsets in a weld subjected to some nominal loading using a full-field surface strain mapping technique. This process makes use of the digital image correlation program (VIC_2D) developed by the University of South Carolina. Full-Field surface strain mapping will be used to help determine the basic material properties of the various regions within a weld, which are the heat-affected zone and the mechanically affected zone (weld nugget).

During development of this process, various specimens were tested to verify the accuracy of the strain mapping procedure. A tapered stainless steel tensile specimen was studied and the results verified by a finite element model of the test specimen. The results from the full-field strain mapping matched very closely with the strain distribution predicted by the finite element model. To further prove the validity of the strain mapping process, a .0135 inch diameter hole was drilled in a 5454-O aluminum tensile specimen. The strain measurement process detected the perturbations in the strain field caused by the defect at displacements as low as three-hundredths of an inch within the three-inch gage length. Furthermore, the strain measured near the edge of the specimen using the mapping technique matched to within .01 % the strain measured by an extensometer attached to the test specimen.

Tests then proceeded on tensile specimens with welds passing transversely through the material. From these tests, stress-strain curves were constructed for the microstructure regions within welds. The stress-strain curve created for the weld nugget matched the one from a standard tensile test on a similar weld specimen. Additionally, stress-strain curves for the heat-affected zone, and the base metal immediately outside the weld, were created. These curves show the mechanical and heat effect of the friction stir welding process on the base metal strength.

Specimens with welds passing through them longitudinally were also examined. These specimens exhibited a uniform displacement field across the surface of the weld indicating uniform strain. A stress-strain curve was created for a longitudinal fusion weld using the strain mapping technique developed during this study. The stress-strain curve created for the longitudinal weld specimen matched the stress-strain curve of the base metal almost exactly.

TABLE OF CONTENTS

LIST OF FIGURES

CHAPTER 1

INTRODUCTION AND BACKGROUND

The various processes for making a welded joint affect the base metal in different ways. Since the temperature of the base metal varies during welding, from melting temperature in the weld (depending on the process) to room temperature in the areas most remote from the heat source, regions of distinctly varying microstructure form due to the welding process and the heat involved. The weld itself is characterized by the microstructure within the weld nugget for a friction stir weld or fusion zone for a fusion weld. Moving outward from the center of the weld into the base metal the microstructure of the heat-affected zone is observed. After the heat-affected zone the microstructure returns to that of the base metal.

Varying microstructure regions such as these give welded materials a wide range of properties that will vary as a function of position relative to the weld. However, the effect of the welding process on the base metal is dependent on the type of material being welded. When steel is involved, the area near to, and in the weld zone, can be heated to a temperature well above the transformation temperature of the steel. This results in a coarse grain structure in the weld and adjacent areas. Hardening of the weld and adjacent base metal, heated above the transformation temperature of the steel, can occur if the steel contains sufficient carbon and the cooling rate is high enough. This is an

undesirable effect in steel in that hardening of the weld zone increases the susceptibility to cracking (Parmley, 1997). Similarly, welding aluminum alloys tends to cause coarsening of the grains in the heat-affected zone, but the result is a softer material. The area of minimum hardness in the heat-affected zone is usually the localization of initial failure regardless of welding variables (Malin, 1995). This may vary depending on the aluminum alloy being welded. In friction stir welds made in aluminum, fine grains have been observed in the weld nugget and adjacent heat affected zone. The lower heat input limits the growth of the grains in the heat-affected zone giving the weld high strength (Haagensen, 1995). The stirring, crushing, and forging action of the welding tool produces a weld metal with a grain structure much finer than the base metal or heat-affected zone. This generally gives the weld metal a greater strength than the heat-affected metal in the as-welded condition (Dawes, 1996).

In order to understand the overall strength of a welded material it is necessary to understand how the various microstructures that make up the weld act under a load. The relative properties of the materials in the different zones that make up a weld will depend on the alloy and on the welding conditions. In addition, changes in properties between zones may be sharp or gradual. Further complications arise when the specimen under study exhibits stress concentrations due to its geometry. Residual stresses created in the weld from the welding process can also have a profound effect on the yield strength of the material. Tensile residual stresses can cause the weld to yield at a substantially lower stress than would normally be observed in pure metal. Conversely, compressive residual stresses could prolong yielding until a substantially higher stress.

The overall goal of this project is to use full field surface strain measurement in combination with an iterative finite element analysis to determine the constitutive behavior of all the microstructure regions of a welded joint. In addition to constitutive data, we hope someday to be able to extract information regarding the state of residual stress existing in a weld by tensile and compressive loading of welds. This information can then be used to modify welding processes to optimize weld properties and to accurately model the mechanical response of welded joints.

1.1 Material Properties of Welds

Numerous techniques have been applied to determine the properties of materials that make up a weld. For instance, relative strength levels in weld regions are routinely determined by mapping the hardness of welded joints. The hardness number, which is a measure of the resistance of a material to penetration by a pointed tool, can then be used with proven mathematical relations to determine several key mechanical properties (Shigley, 1989).

There are many methods for determining the hardness of a material. Most involve using an indentation tool with a known load. The penetration depth of the indentation tool is a measure of the hardness of the material. The Rockwell and Brinell hardness tests are the most widely used. However, Knoop hardness is also a commonly used test because it generates a state of plane strain during the test. This simplifies the stress analysis somewhat because it essentially measures the deformation in only one plane (Meyers, 1984).

Efforts have been made to make indentation-testing methods automated and portable for use on field-welded materials. This system is based on strain-controlled multiple indentations, at the same penetration location, of a polished surface by a spherical indenter. This type of test has the ability to measure mechanical properties such as yield strength, true-stress/true-plastic strain, strain hardening exponent, Luders strain, elastic modulus, and can also allow the local fracture toughness to be estimated. This microprobe test system has been used successfully to nondestructively test in-situ a circumferentially welded Type 347 stainless steel pipe. The test head of the microprobe system was mounted directly onto the pipe being tested allowing a 360 degree inspection of the property gradients in the weld and its heat-affected zone (Haggag, 1993).

1.2 Residual Stress

Heating and cooling due to the welding process can cause residual stresses to be locked into the material being welded. The presence of residual stresses in this materials will effect the mechanical properties regardless of the process used to measure them. As a material is welded, heat from the process causes it to expand locally at the heat source. The welding process captures this elongation by joining the material being welded in its expanded state. The subsequent cooling, and contraction, of the material after the welding process locks in residual stresses that can effect the strength of the weld. A compressive residual stress will increase the strength of the welded joint under a tensile load in the direction parallel to the residual stress. Conversely, a similar tensile residual stress will weaken the joint under a tensile load (Parmley, 1997).

4

1.3 Digital Image Correlation

Digital image correlation is an innovative measurement technique that compares two digitized images to determine the displacement between them (Bruck, 1989). This procedure is also useful in measuring quantities such as velocity, displacement of a cantilever beam, and displacement of a cracked body (Sutton, 1986). The process of acquiring images utilizes a digital imaging system consisting of a stationary video camera and a desktop computer containing a digitizer. To provide adequate contrast for digitizing, a random speckle pattern consisting of various sized random black dots on a white background is applied to the specimen being observed by the video camera. The scale of the pattern depends on the size of the area to be viewed.

An initial undeformed image of the specimen is taken. The specimen is then deformed and another image is taken. This process is repeated until the test is complete or the pattern begins to break down. The initial undeformed image can then be digitally compared to the deformed images to determine the displacement between them. This entire process is performed using a PC based program, VIC_2D, which was developed at the University of South Carolina.

An easy way to think about digital image correlation is that the digitized intensity of the black and white speckle pattern is discrete in nature, and represents only a sampled version of the actual intensity distribution present at the image plane of the camera sensor. This digitized information is stored in two arrays within the computer. The deformation of the object can then be determined by comparing the data within the two arrays if the following assumptions are true. First, it is assumed that the small subsets of the intensity pattern stored in the array containing the data for the deformed image are

related to small subsets of the same size in the array containing the data for the undeformed image by a homogenous linear mapping. Secondly, it is further assumed that this mapping of local subsets of intensity data is the same mapping as that which applies to the deformation of the objects surface which reflected the intensity pattern to the camera sensor (Sutton, 1983). The information stored in each array is a numerical value for each pixel representing its gray level. An eight-bit digitizer, giving intensity data ranging from 0 to 255, is usually used with the lowest value representing black and the highest value representing white. Digital image correlation then becomes a job of comparing subsets of numbers between the two digital images. A typical correlation function, which measures how well the subsets match, has the form

$$S\left(x,y,u,v,\frac{\partial u}{\partial x},\frac{\partial u}{\partial y},\frac{\partial v}{\partial x},\frac{\partial v}{\partial y}\right) = 1 - \frac{\sum (F(x,y)*G(x^*,y^*))}{(\sum (F(x,y))^2 * \sum (G(x^*,y^*))^2)^{1/2}} \qquad (1.1)$$

where F(x,y) is the gray level value at coordinate (x,y) of the undeformed image and G(x*,y*) is the gray level value at point (x*,y*) for the deformed image. The coordinates (x,y) and (x*,y*) are related by the deformation which occurred between acquisition of the two images. If the motion of the object relative to the camera is parallel to the image plane, the coordinates are related by

$$x' = x + u + \frac{\partial u}{\partial x}\Delta x + \frac{\partial u}{\partial y}\Delta y$$

$$(1.2)$$

$$y' = y + v + \frac{\partial v}{\partial x}\Delta x + \frac{\partial v}{\partial y}\Delta y$$

where u and v are the displacements of the subset centers in the x and y directions respectively. The terms Δx and Δy are the distances from the subset center to point (x,y).

6

The most common method of digital correlation involves a coarse-fine search routine to obtain the position of the minimum or maximum of the correlation function. The procedure is simple to program but suffers from a lack of a directional measure that would sense in what direction one should search to obtain the correlation maximum or minimum. As a result there is some question as to whether the solution is an absolute relative maximum or minimum (Sutton, 1986). The coarse-fine search routine is also computationally intensive because it tries many possible combinations of the variables within a given range comparing the correlation factor for each. Because of the large number of calculations this technique requires, it is usually used for determining u and v only (Bruck, 1989).

The Newton-Raphson correlation method is a second order optimization method which can be used together with differential correction to improve convergence speed. This method gives corrections for initial guesses of the six deformation parameters and will converge to the solution with substantially fewer calculations (Sutton, 1986).

Another factor in determining whether the coarse-fine search method or the Newton-Raphson method with partial differential corrections is used is the amount of contrast available in the images. For images of poor contrast the computationally intensive coarse-fine search method is used. When sufficient image contrast is available, the Newton Raphson method is used.

Image correlation is performed by determining values for u, v, $\partial u/\partial x$, $\partial u/\partial y$, $\partial v/\partial x$, and $\partial v/\partial y$ which minimize the correlation coefficient (S). If simple correlation methods are used which are accurate to within one pixel, the results will have errors much greater than the quantities to be measured. The solution to this problem is to

interpolate between pixels and obtain a reconstructed, continuously varying intensity pattern (Sutton, 1986).

Since digital images contain discrete pixel information it is necessary to "smooth" the data to obtain a continuous intensity pattern. Bilinear and bicubic spline interpolations are two methods used in determining subpixel information. For the coarse-fine search method, bilinear interpolation is used. Bilinear interpolation approximates the gray level value at point (x*,y*) which is between the pixels (i,j), $(i+1,j)$, $(i,j+1)$, $(i+1,j+1)$, by

$$G(x^*,y^*) = a_{00} + a_{10}(x') + a_{01}(y') + a_{11}((x')(y'))$$ (1.3)

Where

a_{00} = gray level of pixel (i,j)

a_{10} = gray level of pixel $(i+1,j) - a_{00}$

a_{01} = gray level of pixel $(i,j+1) - a_{00}$

a_{11} = gray level of pixel $(i+1,j+1) - a_{00} - a_{10} - a_{01}$

The x' and y' are the x and y distance from pixel (i,j). It was found greater accuracy could be obtained by using bicubic spline interpolation. The functional form for the gray level at (x*,y*) which is between pixels (i,j), $(i+1,j)$, $(i,j+1)$, $(i+1,j+1)$, using a bicubic spline is

$$\begin{aligned} G(x^*,y^*) = &\, a_{00} + a_{10}(x') + a_{20}(x')^2 + a_{30}(x')^3 + a_{01}(y') + a_{02}(y')^2 + a_{03}(y')^3 \\ &+ a_{11}(x')(y') + a_{21}(x')^2(y') + a_{31}(x')^3(y') + a_{02}(y')^2 + a_{12}(x')(y')^2 \\ &+ a_{22}(x')^2(y')^2 + a_{23}(x')^2(y')^3 + a_{33}(x')^3(y')^3 \end{aligned}$$ (1.4)

where a_{00} is the gray level of pixel (i,j). Using the first order and cross derivatives at nodal locations, the remaining coefficients are determined so that all of the first order and cross derivatives are continuous between adjacent surfaces (Bruck, 1989).

The Newton-Raphson method has some numerical considerations that must be kept in mind when evaluating the results. The first consideration is that the partial corrections are assumed to be small. Therefore, only the first term of the Taylor's series was used in deriving the Newton-Raphson equations. In practice, it has been found that the partial corrections should be less than unity for stability of the algorithm. The second area of concern is when the Newton-Raphson method finds the absolute or the local minimum of the correlation function. The correct solution to a problem will be located at the absolute minimum of the correlation function. Since the Newton-Raphson method finds the minimum using gradients, it is possible for the method to find a local minimum instead of the absolute minimum. For the absolute minimum to be found, the initial guess must be sufficiently close to the true answer. To determine if the initial guess is sufficiently close to the true answer, the standard coarse-fine search method is used . In this method, the displacements of the subset center are estimated to within one pixel. This method was found to give an acceptable initial guess in almost all cases. Finally, the method may converge towards the absolute minimum but the additional correction terms may cause oscillation about the true answer. Typically this oscillation is small, if it occurs at all.

Digital image correlation is an effective tool but the quality of the results is dependent on the quality of the images. Images of low contrast are difficult to correlate and may give results with large errors. As long as there is sufficient contrast, digital image correlation will provide meaningful results with high accuracy (Tolat, 1991). The correlation program, VIC_2D, offers several choices for the user to choose from. Knowledge of the situation, and a good understanding of the correlation process, will

allow the user to make good choices for correlation technique, subset size and initial

guesses.

CHAPTER 2

PROCEDURE AND EQUIPMENT

2.1 Applying the Random Pattern

Several methods were examined for applying the random speckle pattern to the specimens used in this study. Ultimately, the method used to apply the pattern will be dictated by the magnification of the imaging equipment and the material subset size being studied. The most successful methods of pattern application developed during this study are discussed below.

2.1.1 Using Paint

Off-the-shelf spray paint is an inexpensive and simple to use material for application of the random speckle pattern to a test specimen. Patterns applied with this process are adequate when the camera field of view covers 1.5 square inches or more. Preparation of the sample begins by cleaning the specimen and examining its surface finish. If the surface of the specimen is very smooth it needs to be roughened with medium coarse sandpaper. There is no specific procedure for this. The only purpose for this is to give the paint some fine grooves to adhere to. Good adhesion of the paint is important since the specimen will be subjected to a strain. Once the surface has been roughened, the sample is cleaned a final time to remove any residue from sanding.

A moderately thin coat of white paint is applied to the region of interest on the specimen. The thickness of the white paint layer is critical. If the paint layer is too thick it will exhibit poor elastic qualities causing it to crack and "pop" off at very low displacements. The random black speckle pattern is then applied by holding a can of black spray paint about 12 to 18 inches away from the specimen and spraying it with a side-to-side sweeping motion. It is important to always shake the spray paint well and clear the sprayer by releasing paint on an unwanted object before applying it to the test specimen. This will help insure the paint sprayer delivers a uniform amount of paint for even coating. A typical random speckle pattern applied with this process is shown in Figure 1.

A variation of this process utilizes copier toner powder to form the random black speckle pattern. The toner powder gives a significantly finer pattern for use at higher magnifications. In applying this type of pattern, the white background is applied as described above. Instead of allowing the white paint to dry on the specimen it is placed immediately into a specially designed apparatus to apply the toner powder. This apparatus is made of two different sized chambers, a large chamber in which the specimen is placed and a small chamber that contains the toner powder. The chamber containing the toner powder is connected to a compressed air supply via a small tube. The chamber containing the specimen has a small tube connected to it to serve as a vent. This vent allows the toner powder to flow through the chamber containing the specimen. A low enough air pressure is used so that some of the toner powder settles on the specimen and embeds itself in the wet background paint. The exhaust end of the vent tube is placed in a container of water that acts as a filter to prevent the toner powder from

being exhausted into the air. A typical speckle pattern made with this process is shown in Figure 2.

2.1.2 Using Photographic Techniques

When there is an extremely small area of interest on the test specimen, requiring very high magnifications, the previously discussed methods of applying the random pattern are insufficient because the resulting pattern is too coarse. To accommodate requirements for very high magnification, a method of applying a very fine random pattern to specimens was developed. The specimen to be tested is first cleaned with a solvent to remove any oil and dirt. The area of interest on the specimen is then coated with photoresist. A mask, in conjunction with an ultraviolet light source, is then used to apply the pattern.

Applying the photoresist is a critical step in this process. If the photoresist is too thick, it will not retain the detailed features of the mask. If it is applied too thin there will not be enough photoresist to transfer the pattern from the mask. The thickness of the photoresist layer formed on the test specimen is a function of its viscosity. Since the viscosity of the photoresist directly from the container is fairly high it is necessary to dilute it with photoresist thinner. Through trial and error it was determined that the optimum viscosity is obtained by mixing equal parts photoresist and photoresist thinner.

To properly apply the photoresist to the test specimen, the specimen must be spin coated so that centrifugal force will spread the photoresist evenly over the test area. After the specimen is secured in the spin coating apparatus, a drop of diluted photoresist, approximately .25 inches in diameter, is placed at the center of the test area. The

specimen is then rotated at approximately 750 rpm for 10 to 15 seconds to allow the photoresist to spread out and harden. After this process, reasonable precautions should be taken to protect the specimen from direct exposure to light. Otherwise, the photoresist will degrade chemically and will not accept the pattern properly.

Once the specimen has been coated with photoresist, a negative of the pattern is applied utilizing a mask. The mask used in this instance is simply a piece of glass that has had the negative of the desired pattern applied to it. This was done at the Cornell Nanofabrication Facility. Figure 3 shows the center portion of this mask that contains the pattern. To transfer the pattern, the mask is placed over the photoresist so that the portion of it containing the pattern is directly over the area of interest. Small weights are placed on top of the mask to hold it in place and insure there is good contact between it and the photoresist. Both the mask and specimen are then placed under an ultraviolet light source for approximately seven minutes. This transfers the pattern from the mask onto the test specimen by breaking down the photoresist exposed to the ultraviolet light. The photoresist covered by the fine mesh pattern of the mask is protected and remains chemically intact.

After the seven-minute exposure to ultraviolet light the specimen is placed in a bath containing developing solution for 10 to 15 seconds. This removes the photoresist that was exposed to the ultraviolet light but leaves the unexposed photoresist on the specimen. However, care must be taken not to over develop the test specimen. Leaving the test specimen in the developing solution too long will remove the unexposed photoresist as well. After the specimen is removed from the developer bath, it should be rinsed with water immediately to remove any remaining developing solution.

To complete the process, the specimen is boiled for sufficient time to build up a dark oxide layer on the aluminum. After boiling the remaining photoresist is removed with a solvent to expose the bright aluminum underneath. The contrast between the dark aluminum oxide and the bright aluminum is sufficient for correlation. Figure 4 shows the type of pattern produced with this method.

2.2 Data Acquisition

The initial equipment configuration for acquiring images utilized a desktop computer with a DTR image board, a Sony XC-77 CCD camera with a 200 mm Cannon variable zoom lens, and two 2X extension tubes. The VIC_2D image acquisition software developed at the University of South Carolina was used with this system. The camera was set up approximately 8 feet away from the specimen in order to compensate for any out of plane motion of the specimen. This gave a field of view of approximately 1.5 square inches at the 100-mm zoom mark.

In an effort to increase the resolution of the system the imaging board in the desk top computer was changed to a digital raptor board and the camera was upgraded to a Pulnix TM-9701 digital camera. A Cannon 200-mm fixed zoom lens with one 2X-extension tube was used with this camera. Once again, the camera was located about 8 ft from the specimen to obtain a field of view of approximately 1.5 square inches. Again, the VIC_2D image acquisition software was used.

2.3 Image Correlation

The analysis of the images acquired with the procedure described in section 2.2 was done using the VIC_2D digital image correlation program developed at the University of South Carolina. The program has several choices the user can select from to tailor the correlation process to the situation being studied. For this study, where the specimen being studied experienced a strain, the image correlation program was set to use the Newton-Raphson correlation method with full partials. Using full partials increased the time required to correlate the images but also increased the accuracy of the correlation. This increase in accuracy is due to the "full partials" setting allowing the program to account for any change in subset shape from the undeformed image to the deformed image.

In the "factor calculation" box there are two choices of when the correlation program will calculate the bilinear interpolation factors. Since the correlations being done on the tensile specimens will always involve more than 10 subsets the "before analysis" option was chosen under the factor calculation block.

The cross correlation option was selected in the correlation measure block. Cross correlation normalizes the error so that is always between zero and one. Also, the cross correlation function has the added advantage of making the correlation process less sensitive to lighting changes.

Because the Newton-Raphson method has a tendency to diverge if the initial guess is too far from the correct solution, VIC_2D has the capability to switch into coarse-fine correlation if the error from the Newton-Raphson method becomes too large. The coarse fine factor block tells the image correlation program when to switch from the

Newton-Raphson method to coarse-fine correlation. The value assigned in this block normally can range between .005 and .02. The correct factor can change between tests because the ability of the program to match subsets accurately changes with the quality and contrast of the pattern. For the specimens tested during this study a coarse-fine factor of .01 was usually used.

The coarse-fine range designates how large of an area will be searched using coarse-fine correlation. The larger the number the bigger the area. The penalty for a large area is a dramatic increase in the amount of time required for calculation at each point. In general, a value of 10 is a good compromise between correlation time and a reasonable assurance that the search will include the best-fit location. Ten was the value used for all correlations in this study.

2.4 Determination of Strain

The strain was determined from displacement data obtained from the digital image correlation procedure discussed in section 2.3. The displacement that was directly determined by the correlation process was plotted for constant Y paths longitudinally along the specimen. A curve was fit to this displacement data using Sigma Plot 4.0 that resulted in an equation for displacement as a function of X. The derivative of the displacement equation will give the strain as a function of X for the constant Y path chosen.

CHAPTER 3

PROCESS DEVELOPMENT

3.1 Methodology Verification Tests

In order to verify the methodology of making full field strain measurements on tensile specimens under load, two specially prepared specimens were tested. The first was a stainless steel specimen with sides that taper into a narrow center section. The second was a standard aluminum tensile specimen with a .0135 inch diameter hole in the center. A finite element model of the stainless steel tapered specimen was used to verify the results that were obtained from digital image correlation. The verification test procedures are discussed below in detail.

3.2 Tapered Stainless Steel Specimen

The objective of this test was to verify that the image acquisition system and digital image correlation could accurately detect displacements in a test specimen with varying geometry. For this test a tensile specimen with tapering sides and a narrow midsection was machined from stainless steel. Figure 5 shows this tensile specimen with the random black and white speckle pattern applied. This experiment attempts to simulate the varying properties of welded regions due to the differing microstructure caused by welding processes.

In preparing the specimen for the test, it was first cleaned to remove any grease and oil left over from the machining process. The random speckle pattern was then applied using black and white spray paint as discussed in section 2.1.1. Since an extensometer could not easily be attached to the specimen a one-inch gage length was marked on it using calipers. This gage length will provide a means for accurately determining the total displacement the specimen experienced from the images to be correlated. This measured displacement will be important for the finite element verification that will be discussed in section 3.3.

The video imaging system was set up for this test using a Pulnix TM-9701 digital camera and a Cannon 200-mm lens with a 2X-extension tube as described n section 2.3. The camera was placed approximately eight feet away from the sample being observed. This is sufficient distance so that the effect of any "out-of-plane" motion due to the sample being slightly deformed from the machining process would be minimized. The tensile specimen was then placed in a servo-hydraulic material testing machine and deformed under displacement control. Images were taken at regular intervals of ram displacement for consistency only. Due to slippage of the grips during the initial loading, and the deformation of the columns on the materials testing machine, the ram displacement data bears no relation to the displacement of the tensile specimen.

The images that were obtained were correlated using the digital image correlation program VIC_2D with the program settings specified in section 2.3. The displacement contour plot obtained from the correlation of the undeformed image with one of the deformed images is shown in Figure 6. This plot shows that the majority of the displacement is confined to the narrow center portion of the specimen. It is also observed

that the displacement is higher on the outside edges than in the middle. This is evident from the slightly larger spacing between the displacement contours at the centerline near the 200 and 550 positions on the X-axis. From the data that generated the displacement contour graph, a plot of displacement versus X position was created for three constant Y positions on the specimen. Figure 7 shows this data. Again, it is evident that most of the displacement occurs in the narrow portion of the sample. It is, however, not as evident that the displacement is greater along the outside edges of the specimen than it is along the centerline.

The strain in the specimen along these constant Y positions can be obtained by fitting a polynomial curve to the displacement data and taking the first derivative of the resulting polynomial. Figure 8 shows a plot of the strain obtained from this procedure versus X position along the specimen.

3.3 Finite Element Verification on Tapered Stainless Steel Specimen

In order to verify the results obtained from digital image correlation on the tapered tensile specimen a finite element model was developed and analyzed utilizing ABAQUS software from Hibbitt, Karlsson, & Sorensen, INC. The ABAQUS input file for this model is given in Appendix I. For the development of this model plane stress conditions were assumed to exist in the test specimen. That is, all stresses in the Z direction are assumed to be zero. The material properties for the tensile specimen were simulated using the elastic and plastic models in ABAQUS. These models are used to describe the elastic and inelastic flow of metals at temperatures where creep effects are not important. The elastic model requires only that Young's modulus and Poisson's ratio

be known for the material being modeled. The plastic model requires that the stress-strain curve for the material being modeled be converted into true stress and true strain. Also, the true elastic strain must be subtracted from the total true stress-strain data so there will be an apparent true strain of zero at the yield point. This adjusted stress-strain information is then entered into the ABAQUS input program under the "Plastic" heading.

The finite element model will require the actual displacement experienced by the test specimen to be entered into the input program. This was determined by first measuring the number of pixels in the gauge length on the undeformed image using a photo-editing program. From this it was determined that there were 519 pixels in the one-inch gage length. The number of pixels between the gage marks on the deformed image was measured to be 546. This gave an increase of 27 pixels in the deformed gage length, which was multiplied by 1-inch/519 pixels to determine the actual displacement the specimen experienced. Using this method the actual gage length displacement was calculated to be .052 inches.

To physically model the tensile specimen, a finite element mesh was initially designed that contained 2193 nodes, which is shown in Appendix II. This mesh was laid out with an increased node density in the gage region of the specimen and was designed for use with eight-node biquadratic elements with full integration. The finite element model was evaluated and values for both longitudinal stress and strain were obtained and plotted for nodes corresponding to the constant Y paths through the actual test specimen. This input file required approximately ten minutes to execute on a 200 MHz desktop computer.

To assure that the finite element model was giving accurate stress-strain values, a six-node triangular element with full integration was substituted for the eight-node element. This triangular element divided each of the original square elements in half thus doubling the number of elements. This model was evaluated and values for longitudinal stress and strain obtained. These values were plotted for the nodes that related to the constant Y paths through the actual test specimen. Again, this input file required approximately ten minutes to execute on a 200 MHz desktop computer.

To be certain that the finite element model had converged to an accurate solution the mesh was refined. In doing this refinement, the number of nodes in the mesh was increased from 2193 to 8085. Again, values for longitudinal stress and strain were strain obtained and plotted for the nodes relating to the constant Y paths through the actual test specimen. This input file required approximately thirty minutes to execute on a 200 MHz desktop computer.

The results from these three separate evaluations of the finite element model were plotted. Figures 9 and 10 show the results from these three models for strain, which is the secondary variable in the finite element model. Strain is the secondary variable since it is calculated based on the stress calculated by the finite element model. It is important to examine the secondary variable since it is least likely to converge. Figures 11 and 12 show the results for stress, which is the primary variable for the finite element model. The primary variable because it is calculated directly by the equations in the finite element model. As can be seen, all models gave approximately the same result indicating they had converged to a solution. This implies that no further refinement of the mesh is

required. Therefore, the first model will be used for comparison with the digital image correlation results.

For the axial centerline of the specimen, the ABAQUS data and the digital image correlation data matched well. The data for the outside edges varied in that digital image correlation predicted a peak and the finite element model predicted a region of near constant strain. This can be seen in Figures 13 and 14 which show the strain data obtained from digital image correlation superimposed on the strains obtained from the finite element model.

The differing results could be due to several factors. The fact that the finite element model was a two dimensional model and the specimen was three-dimensional could be a reason for the difference. Also, inaccuracies in the finite element program in dealing with edge effects could have an effect on the results. Additionally, the averaging effect of digital image correlation process could have an effect on the data.

3.4 Aluminum Specimen with .0135 Inch Diameter Hole

The purpose of this experiment was to determine if the displacement contours around a small defect in a material could be detected. For this test, a standard tensile specimen, .075 inches thick, of 5054 aluminum was machined and a .0135 inch diameter hole drilled in its center. A .0135 inch diameter hole was chosen to model a material defect in the test specimen because .0135 inch is the smallest diameter drill bit that would drill through the specimen without breaking. Figure 15 shows the random black and white speckle pattern around the hole. The .0135 inch diameter hole can be seen in the

center. Because of the small area of the sample being observed, the random pattern was applied using toner powder as described in section 2.1.1.

After the imaging equipment was set up, the tensile specimen was placed in the servo-hydraulic material testing machine and deformed longitudinally using displacement control. Images were take at regular intervals of displacement for correlation using the Sony XC-77 CCD camera and desktop computer with a DTR board. The images were correlated using VIC_2D with the correlation settings described in section 2.4.

Figure 16 shows the contours of displacement in the longitudinal direction along the specimen. This displacement map was obtained at a nominal strain of .0428 in/in as measured by the attached extensometer. The variation in the displacement contours around the hole can be readily observed. The gathering of the contours in the vicinity of the hole indicate that digital image correlation is sensitive to the displacement concentrations caused by geometrical irregularities. Additionally, when the displacement data for the edge of the tensile specimen, where the extensometer was attached, is isolated and analyzed, the resulting strain matches almost exactly that measured by the extensometer. Figure 17 shows a plot of the displacement data that was isolated for this edge. A linear equation was fit to this data. The derivative of this equation revealed a constant strain equal to .0427 in/in whereas the extensometer measured .0428 in/in. This excellent correspondence between the extensometer and digital image correlation strain measurement is further evidence of the validity of the technique.

CHAPTER 4

PROCESS APPLICATION

The following tests were conducted on specimens made from friction stir and fusion welds utilizing the method for making full field strain measurements discussed in Chapter 3. Specimens with both transverse and longitudinal welds were examined using the strain measurement technique developed during this study. This method of strain measurement will make possible the determination of the constitutive properties for the different microstructure regions making up the weld itself. Being able to determine these basic properties of the material that make up the weld will provide a measure for optimization of the welding process. Welding parameters can then be selected to achieve a weld with the desired mechanical properties.

4.1 Transverse Welds

In transverse weld specimens, the weld direction is perpendicular to the direction of loading. In this type of specimen the regions where the microstructure varies within the weld is analogous to a composite material assembled in series. The base metal is present on each end with the heat-affected zone on each side of the weld nugget. This configuration is similar to the iso-stress condition found in composite material (Reynolds, 1998).

Full field strain measurements were made on the top, bottom, and side surfaces of transversely oriented friction stir welds. Welds examined in this test were made in 5454-O and 5454-H-32 aluminum. Additional tests were conducted on friction stir welds made in 5454-H32 aluminum for which the tool rotation speed was varied from weld to weld. The results of these tests are discussed below.

4.1.1 O-Temper Aluminum Friction Stir Weld

5454-O aluminum was used in the first attempt at creating a friction stir weld at the University of South Carolina because it is a relatively soft aluminum with low yield strength. This made it easier to work with during the initial setup of the welding process and decreased the risk of tool damage if a mistake was made. Standard tensile tests on these welds indicated that the weld material had essentially the same stress-strain response as the base metal.

Tensile tests were then conducted on weld specimens in which digital image correlation was used to measure the strain. The top, bottom, and side surfaces of these weld specimens were examined. To prepare the test specimens used here, the random black and white pattern was applied using spray paint as described in section 2.1.1. Following a procedure similar to that used in the verification tests of Chapter 3, the specimen was placed in a servo-hydraulic material testing machine and deformed under displacement control. Images were taken when the specimen had experienced approximately 1 % strain. A low strain level was targeted in this test to determine if there were any strain localization within the weld this could be detected at low loads.

Choosing a uniform strain level for all tests also allowed the results from all three tests to be compared.

Digital image correlation on the top surface of the weld revealed a near uniform displacement across the surface. A plot of the displacement versus longitudinal (X) position on the weld is shown in Figure 18. The curves shown represent three constant Y longitudinal paths through the weld. A ninth order polynomial curve was fit to the displacement data in Figure 18. The derivative of the resulting polynomial provided the strain along these constant Y paths, which is shown in Figure 19. As expected, they also indicate a relatively uniform strain distribution across the face of the specimen. It is important to notice that the maximum strain for the top surface of the weld, approximately 1.7 %, is near the center of the weld along the longitudinal path.

Tests were performed on the back surface of the weld using the same procedure that was used for the top. Figure 20 shows the displacement versus X position for three constant Y paths longitudinally along the surface corresponding to the constant Y paths on the top. As before, a ninth order polynomial curve was fit to the displacement data and the derivative taken to obtain the strain. Figure 21 shows a plot of the strain obtained from the derivative of the polynomial. This data indicates that the maximum strain, approximately 1.7 %, is in the heat-affected zone on either side of the weld center. The center of the weld experiences a relative minimum strain of approximately .4 %.

The next test conducted was on the side of the weld. In this test, the non-homogenous microstructure caused from the welding process will be encountered. Figure 22 shows the microstructure variation through the weld produced by the welding

27

process. Etching the weld area using the Barker's etch method exposed the varying microstructure evident in this image.

Digital image correlation on the side of the weld, performed as described for the top and bottom surfaces, produced the displacement data shown in Figure 23. Again, three longitudinal paths along the weld surface, which correspond to the weld top, longitudinal centerline, and bottom, were isolated for analysis. It is observed that left of the transverse weld center, the bottom of the weld undergoes more displacement than the top. The opposite is true to the right of the weld center. This could be significant in that the left part of the weld is affected by the leading edge of the welding tool and the right part of the weld is affected by the trailing edge.

The strain for the side surface was obtained from the displacement data with the same procedure used for the top and bottom surfaces. Figure 24 shows the strain obtained for the constant Y paths along the surface. Note there is approximately .7 % difference in strain level between the bottom and the top of the weld at the weld center. However, this strain distribution is what was expected based on the Knoop hardness data for this weld shown in Figure 25. It is evident that areas of relatively low hardness experience the highest strain. Additionally, the fact that the strain distribution obtained from digital image correlation corresponds so well to the hardness data serves as further verification that the process of full field strain measurement developed in this study is accurate.

4.1.2 H-32 Aluminum Friction Stir Weld

A test was conducted on 5454-H32 aluminum, which is a strain hardened version of the 5454-O aluminum used in the previous test. The objective of this was to examine the effects of the friction stir welding process on the strain hardened microstructure of the aluminum alloy. Again, the testing procedure described in section 4.1.1 was used. Digital image correlation on the top surface of the weld again showed a near uniform displacement field across the weld surface. This can be seen Figure 26, which shows the plot of displacement versus longitudinal position for three constant Y paths along the top surface of the weld. The strain resulting from the derivative of the ninth order polynomial is shown in Figure 27. Similar to the weld made in 5454-O aluminum, the maximum strain, approximately 2.7 %, occurs near the weld center.

Digital image correlation on the bottom of this weld again showed a uniform displacement field across the bottom surface. Figure 28 shows the displacement data obtained from digital image correlation. The strain derived from a ninth order polynomial curve fit to this data is shown in Figure 29. Once again, the trends in the strain data are similar to the corresponding strain in the 5454-O aluminum. The maximum strain, approximately 2.5 %, occurs on either side of the weld center. The weld center experiences a lower strain level of approximately 1.4 %.

The side of the 5454-H32 weld also exhibited trends similar to the 5454-O. Figure 30 shows the microstructure of the 5454-H32 weld revealed by etching the specimen using Keller's etch method. The displacement data from digital image correlation, shown in Figure 31, indicated that the bottom of the weld experiences a higher displacement than the top of the weld on the leading edge side. The opposite is the case for the trailing

edge side. This is similar to the 5454-O weld. The strain data in Figure 32, which was determined as before, shows the strain distribution through the thickness of the weld as a function of longitudinal position. Once again it can be seen that the top of the weld at the center experiences the highest strain while the bottom of the weld has a lower strain at the center. The strain variation, shown in Figure 32, between the top and bottom of the weld is about 1 %. This strain variation also corresponds to the hardness data, shown in Figure 33, for this type of weld.

However, there were subtle differences between the two welds. The point at which all of the displacements are equal is shifted slightly towards the trailing edge side of the weld. Additional differences can be seen in the microstructure of the two welds. For instance, recrystalization of the microstructure in the heat-affected zone can be seen in the 5454-H32 weld while very little recrystalization occurs in the 5454-O weld. Additionally, the grain size within the weld nugget is larger in the 5454-O weld than in the 5454-H32 weld.

4.1.3 H-32 Aluminum Friction Stir Welds Made With Varying Spindle Speeds

The objective of this test is to detect the stress-strain response of the various microstructure regions present in welds. If the stress-strain response of these regions can be detected, the data obtained can be used to construct stress-strain curves for each microstructure region. This will be a step towards determining the constitutive properties of the weld.

For this study, tests were conducted on welds made in 5454-H32 aluminum with a material feed rate of 3.4 inches per minute and varying spindle speed. Test weld numbers

29 and 30, made at the University of South Carolina, were used. Weld number 29 was made with a spindle speed of 270 revolutions per minute (rpm) while weld number 30 was made with a spindle speed of 750 rpm. Because of the mechanical nature of the welding process, a higher spindle speed causes higher temperatures during the welding process. Therefore, the base metal, just outside the weld zone on weld 30, reached a higher temperature than the base metal in the same relative location on weld number 29. This will be an important fact in interpreting the results of this test.

Because the differing microstructure regions are of primary interest in this test, only the sides of the specimens need to be analyzed. The analysis begins by applying the random pattern necessary for digital image correlation as described in section 2.1.1. Black and white spray paint was used to create the pattern for this test. Once the pattern was applied, a weld specimen was placed in a servo-hydraulic material testing machine and loaded under displacement control. Images were taken at regular intervals of ram displacement so they could be related to the stress level observed by the materials testing equipment. This process was then repeated for the second weld specimen.

The images were correlated using VIC_2D with the settings specified in section 2.4. To obtain enough data to construct a stress-strain curve for the microstructure regions all of the useable images from these tests were correlated. The displacement data obtained from the correlation process for the longitudinal centerline of the weld was isolated and a ninth order polynomial curve was fit to it. To obtain the strain, the first derivative of the resulting polynomial was taken.

Since the stress-strain response for the weld nugget, heat-affected zone, and base metal were of primary concern, strain data for the longitudinal positions corresponding to

these regions were isolated and plotted. The stress-strain response for 5454-H32 and 5454-O aluminum were also plotted on the same graph for comparison. Figure 34 shows the stress-strain response curves for the different microstructure regions in weld number 29. It can be seen in this plot that the stress-strain response for the weld nugget corresponds very closely to the stress-strain curve for the 5454-O aluminum. The microstructure in the heat-affected zone also closely follows the 5454-O stress-strain curve but initially exhibits a slightly higher resistance to yielding than the weld nugget. The stress-strain response of the base metal immediately outside of the weld zone more closely approaches that seen for 5454-H32 aluminum. While the base metal of the weld is 5454-H32 aluminum, the heat it experienced during the welding process slightly degraded its strength.

The same type of plot for weld number 30 can be seen in Figure 35. Once again, the stress-strain response of the weld nugget and the heat-affected zone closely follow that observed for 5454-O aluminum. The noticeable difference in this weld is the stress-strain response of the base metal immediately outside the weld zone. Since this weld was made with a higher spindle speed the base metal should have experienced a higher temperature due to the welding process. The fact that the base metal strength just outside the weld zone for weld number 30 is lower than that observed in weld number 29 for the same region verifies the higher temperature. Additionally, the grain size in the weld nugget of weld number 30 is much larger than the grain size in the weld nugget of weld number 29. This is due to the higher temperatures, produced from the higher rotation speed of the welding tool, which provided for faster grain growth.

To further examine the differences between the two welds, the stress-strain curves for the three different microstructure zones were plotted together. Each of these plots also contains the stress-strain data for 5454-O and 5454-H32 aluminum for comparison. Figure 36 shows the weld nuggets for the two welds. Both weld nuggets exhibit approximately the same properties and closely follow the stress-strain response of 5454-O aluminum. However, there is a subtle difference with the nugget of weld number 29 being slightly stronger.

Figure 37 shows the heat-affected zones of each weld and the stress-strain response of both 5454-O and 5454-H32 aluminum plotted for reference. While the stress-strain response of 5454-O aluminum is still a fair approximation for both heat-affected zones, the heat-affected zone of weld 29 is significantly stronger than the heat-affected zone of weld 30.

Figure 38 compares the base metal immediately outside the weld zone for both welds. The only effect from the welding process experienced by this material was heat. This difference in heat made a significant difference in the strength of the base metal. The higher heat experienced by weld number 30 lowered the yield stress by approximately 9000 psi compared to the yield stress of the base metal in weld number 29.

It is important to note that the stress-strain curves for the 5454-O and the 5454-H32 aluminum used for comparison in this test were created from a tensile test using an extensometer. Additionally, standard tensile tests performed on specimens from these welds all yielded stress-strain curves similar to 5454-O aluminum. The close correspondence of the stress-strain curve generated from digital image correlation on the

weld specimens to the 5454-O curve serves as further validation for this procedure of measuring strain.

4.2 Longitudinal Fusion Weld

The weld used in this test was a tungsten-inert gas fusion weld joining two different thickness of 5454-O aluminum. Figure 39 shows this specimen after completion of the test. This test was conducted to model a weld in a way similar to an iso-strain condition for composite materials. A large field of view was needed because of the size of the specimens being tested. To achieve this it was necessary to move the camera further away from the specimen. Approximately 12 feet of distance was required to achieve the field of view required. Only the top was tested for this study. The top of the weld was characterized by an uneven thickness across the surface.

Black and white spray paint was used to apply the coarse pattern needed for this test. This pattern was applied using the technique discussed in section 2.1.1. The specimen was places in a servo-hydraulic material testing machine and deformed under displacement control. Images were taken at regular intervals of ram displacement so they could be matched to the stress data acquired by the testing equipment.

Digital image correlation, performed as described in section 2.4, was performed on the images acquired. All images correlated displayed a uniform displacement field across the weld surface. Figure 40 shows the uniform displacement field obtained.

The uniform displacement across the surface of this specimen translated into uniform surface strain. Displacement data for a longitudinal constant Y path was isolated

for all the images. An example of the data obtained by this is the constant slope line shown in Figure 41. A second order curve was fit to the data in Figure 41and the derivative taken to obtain the strain. The strain data obtained from digital image correlation was matched to the stress data from the material-testing machine. Figure 42 shows the stress-strain curve created from this process plotted against the stress-strain data for 5454-O aluminum. It can be seen from this plot that the stress-strain behavior of the weld specimen closely matched the behavior of the 5454-O aluminum.

CHAPTER 5

CONCLUSIONS AND RECOMMENDATIONS

5.1 Conclusions

The process for making full-field strain measurements used during this study has been shown to be very successful. Tests conducted indicate that digital image correlation can accurately detect the displacement variations in specimens with varying geometry. This is an important result since the welds ultimately to be studied will contain non-uniform microstructure exhibiting differing stress-strain responses. The results obtained from digital image correlation on the tapered specimen were compared to those from a finite element model of the test specimen. Results from both agreed exceptionally well. Additionally, test conducted to determine if small material defects could be detected showed those strain concentrations from defects as small as a .0135 inch diameter hole could be detected at very low displacements.

Based on the results of the verification tests the method of making full-field strain measurement is considered a viable procedure. Therefore, tests proceeded on specimens made from welded material. As expected, a non-uniform strain distribution was detected longitudinally through the weld zone. Further tests provided data for the construction of stress-strain curves for the microstructure within the weld. The effect of heat on the base metal immediately outside the weld zone could be observed. The more heat that was

created by the welding tool at higher rpm the weaker the base metal became. The same trend was observed for the heat-affected zone. However, the stress-strain response of the weld nugget remained essentially constant. Additionally, the stress-strain curve obtained for both weld nuggets agreed almost perfectly with the results from tensile tests on 5454-O tensile specimens. All of the results discussed above indicate that accurate full-field strain measurements can be made and then be used to determine the material properties of the weld microstructure.

5.2 Recommendations

Although this study has shown that the method developed for making full-field strain measurements gives very accurate results, there are areas for improvement. First, a method for moving the camera automatically in sequence with the weld specimen would increase the accuracy of the stress-strain curves created by this measurement technique. Accuracy would be improved by maintaining the same field of view from image to image. This would help ensure that the measured strain for the exact same point in each image was used to create the stress-strain curve.

Another way of improving the accuracy of this process is to develop a method for fitting a more accurate curve to the displacement data obtained from digital image correlation. The curve fit routine used in this study fits a curve to all of the data at the same time. This method loses some of the fine detail within the displacement data. A method that fits a curve to five or ten data points at a time would retain more of the detail and give more accurate strain measurements.

Finally, a method of automatically taking images at desired ram positions would make this process more user friendly and improve accuracy. Taking images automatically would allow the stress measurements made by the materials testing equipment to be more accurately matched up to the corresponding image. The lag time between when the displacement shown on the materials testing equipment display is read and then the image of the test specimen is taken could be eliminated. Therefore, each image could be matched exactly to its corresponding stress level.

REFERENCES

(Bruck, 1989) - Bruck, H. A., S. R. McNeill, M. A. Sutton, and W. H. Peters III, "Digital Image Correlation Using Newton-Raphson Method of Partial Differential Correction," Experimental Mechanics, Volume 29, September 1989, pp. 261-267.

(Dawes, 1996) - Dawes, C. J., W. M. Thomas, "Friction Stir Process Welds Aluminum Alloys," Welding Journal, March 1996, pp. 41-45.

(Haagensen, 1995) - Haagensen, J. P., O. T. Midling, M. Ranes, "Fatigue Performance of Friction Stir Butt Welds on a 6000 Series Aluminum," Surface Treatment Effects II, 1995, pp.240-253.

(Haggag, 1993) - Haggag, F. M., "In-Situ Measurements of Mechanical Properties Using Novel Automated Ball Indentation System," Small Test Techniques Applied to Nuclear Reactor Vessel Thermal Annealing and Plant Life Extension, American Society of Testing and Materials, 1993, pp.27-44

(Malin, 1995) - Malin, V., "Study of Metallurgical phenomena in the HAZ of 6061-T6 Aluminum Welded Joints," Welding Research Supplement, September 1995, pp. 305-318.

(Meyers, 1984) - Meyers, M. A., K. K. Chawla, Mechanical Metallurgy, Prentice-Hall, Inc., 1984, pp.612-618.

(Parmley, 1997) - Parmley, R. O., "Welding," Standard Handbook of Fastening and Joining, McGraw-Hill, Inc., 1997, pp. 6.3-6.57.

(Reynolds, 1998) - Reynolds, A. P., F. T. Duvall, S. R. McNeill, M. A. Sutton, "Multi-scale Full Field Strain Measurement on Loaded Aluminum Alloy Welds," to appear in the Proceedings of ASM International, 5th Conference on Trends in Welding, June 1998.

(Shigley, 1989) - Shigley, J. E., C. R. Mischke, Mechanical Engineering Design, McGraw-Hill, Inc., 1989, pp.196-199.

(Sutton, 1983) - Sutton, M. A. W. J. Wolters, W. H. Peters, W. F. Ranson, and S. R. McNeill, "Determination of Displacements Using an Improved Digital Correlation Method," Computer Vision, Volume 1, Number 3, August 1983, pp.133-139.

(Sutton, 1986) - Sutton, M. A., M. Cheng, W. H. Peters, T. J. Chao, and S. R. McNeill, "Application of an Optimized Digital Correlation Method to Planar Deformation Analysis," Image and Vision Computing, Volume 4, Number 3, August 1986, pp.143-150.

(Tolat, 1991) - Tolat, A. R., S. R. McNeill, M. A. Sutton, "Effects of Contrast and Brightness on Subpixel Image Correlation," IEEE, 1991, pp. 604-608.
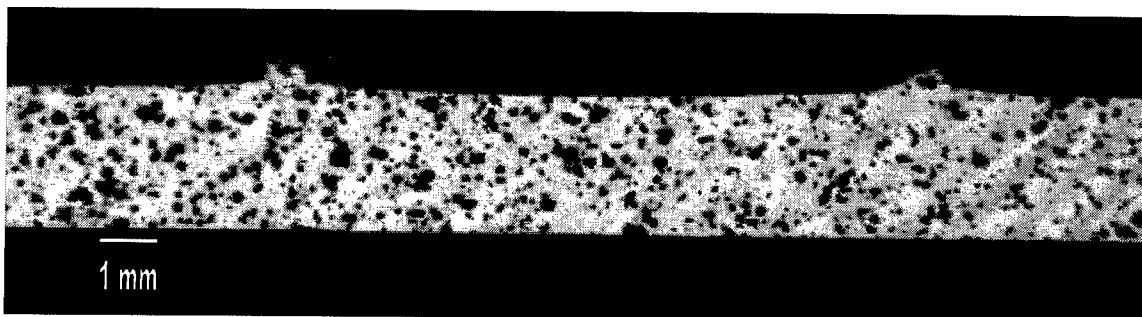
Figure 1: Random Speckle Pattern Created Using Black and White Spray Paint.
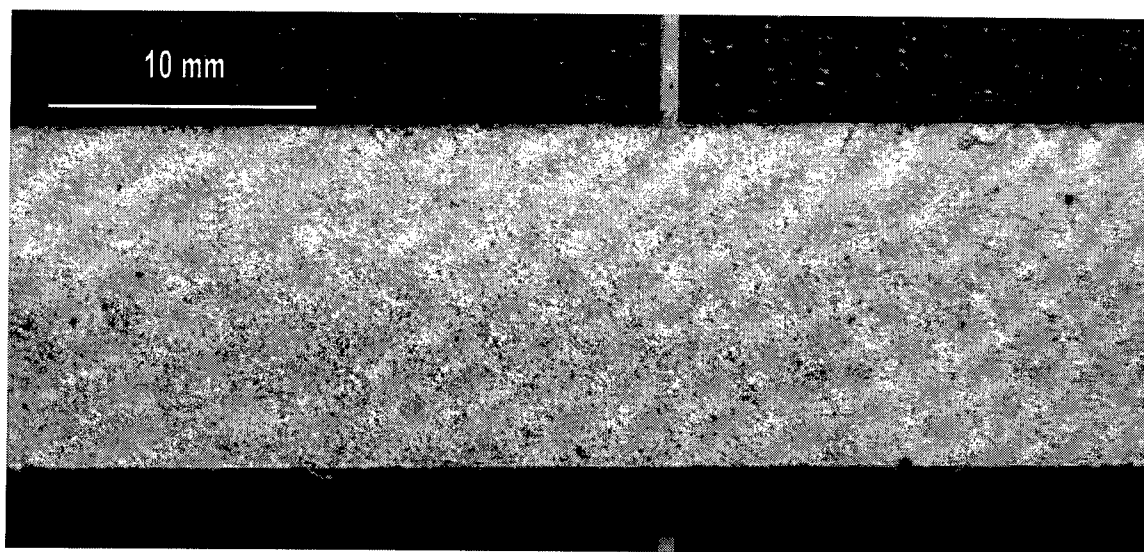
Figure 2: Random Speckle Pattern Created using White Spray Paint and Copier Toner.

41
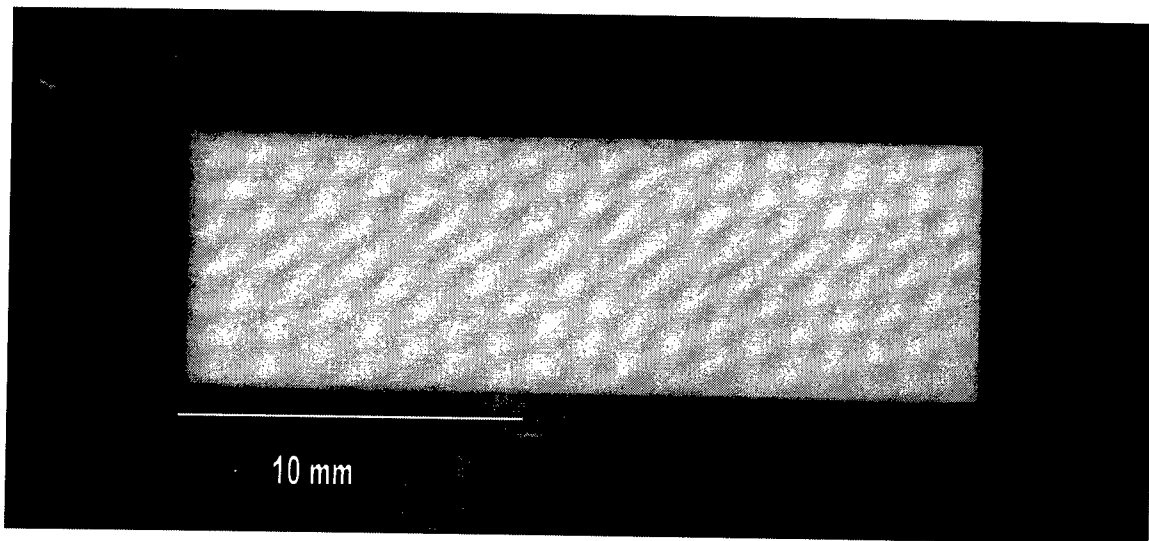
Figure 3: Photographic Mask Used to Apply Random Pattern.
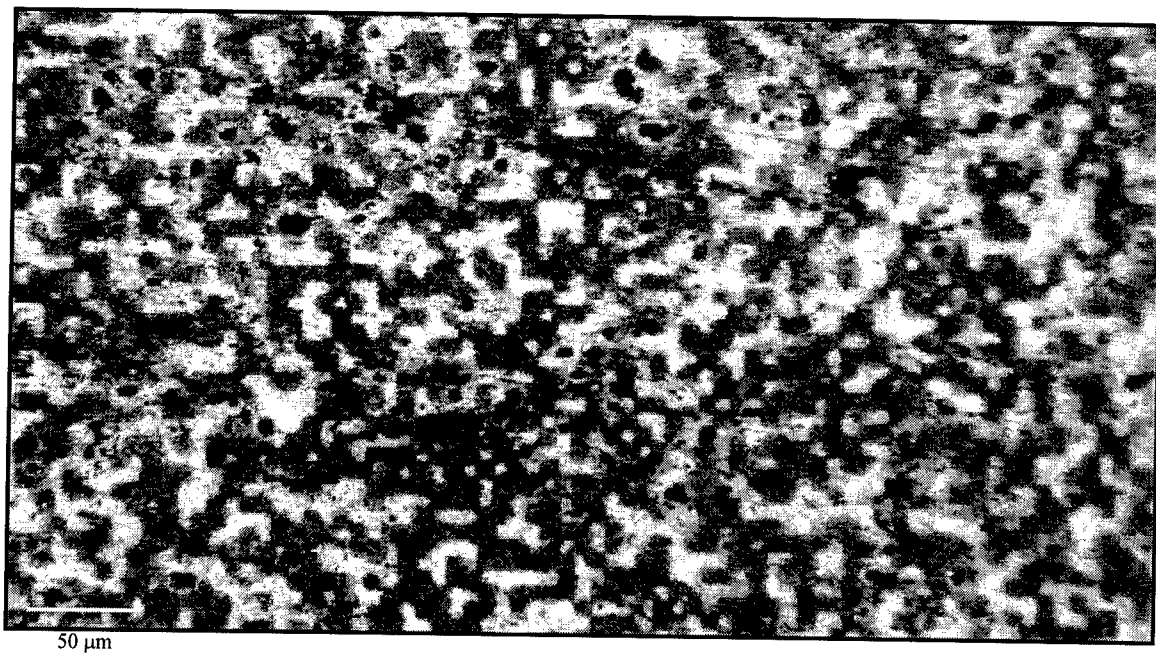
Figure 4: Random Pattern Produced Using Photographic Techniques (magnified 20 times).
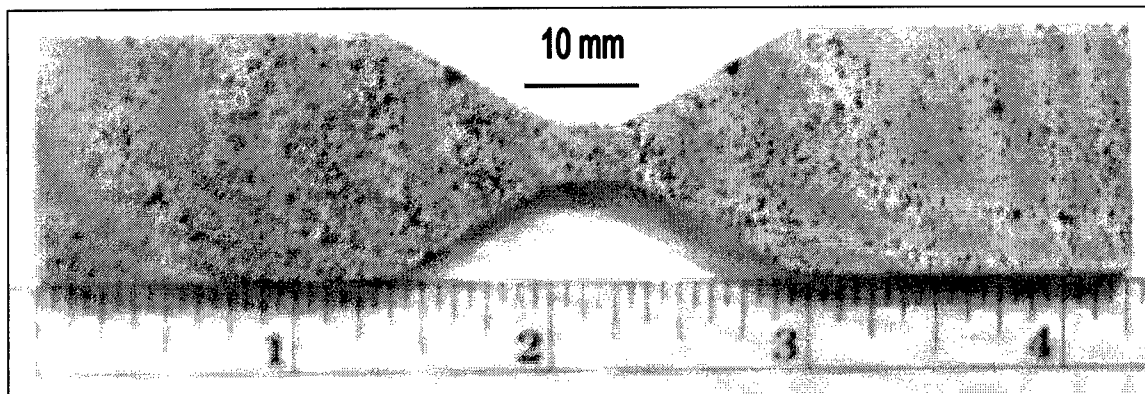
Figure 5: Stainless Steel Tensile Specimen with Tapered Sides.
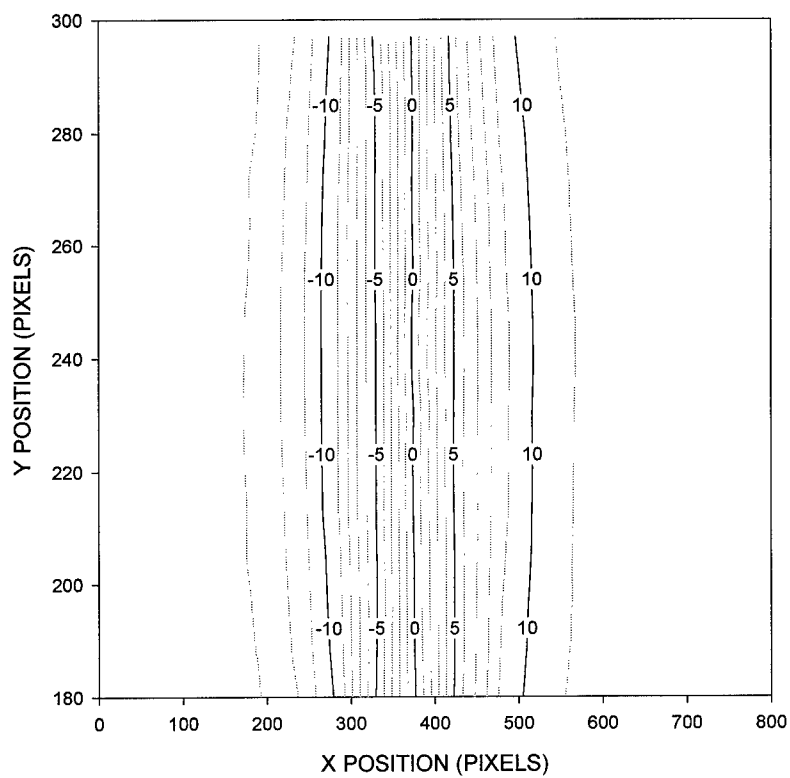
Figure 6: Contour Plot of Displacement for a Gauge Length Displacement
of .052 Inches.

43
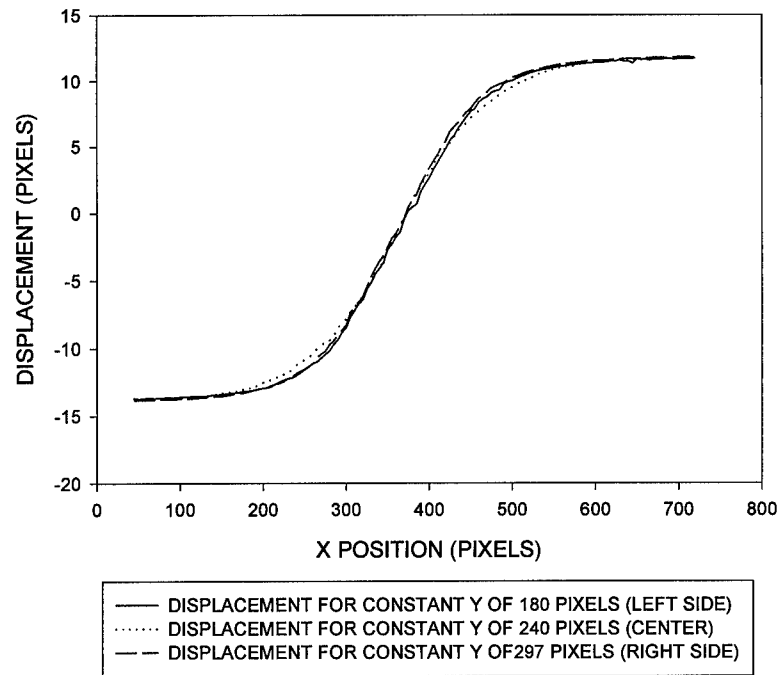
Figure 7: Plot of Displacement Versus X Position for Three Constant
Longitudinal Paths along the Surface of the Tapered Tensile
Specimen.
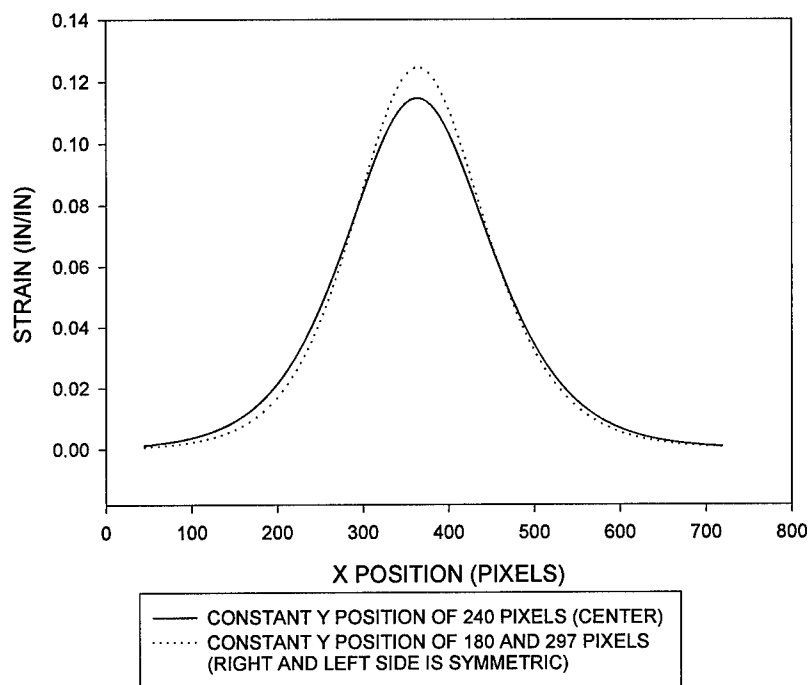
Figure 8: Plot of Strain Versus X Position for Three Constant Longitudinal
Paths along the Surface of the Tapered Tensile Specimen.
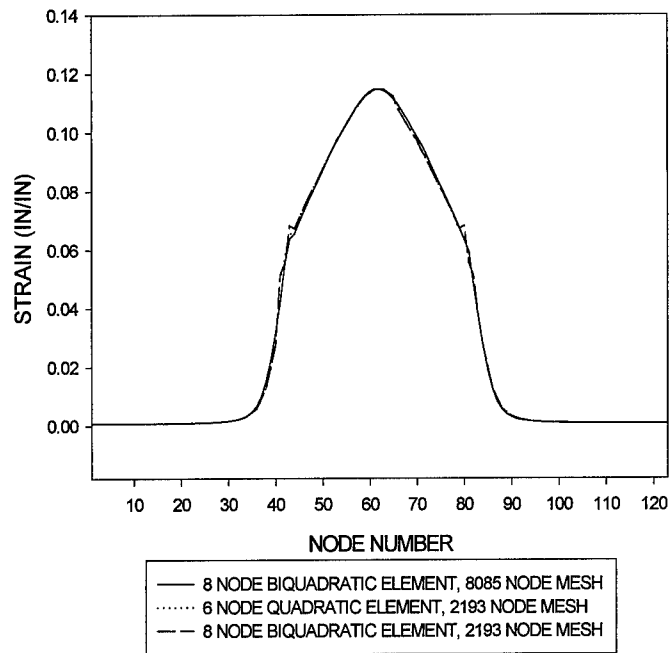
Figure 9: Strain Predicted by the Three Different Finite Element Models
of the Tapered Tensile Specimen along the Longitudinal Centerline.
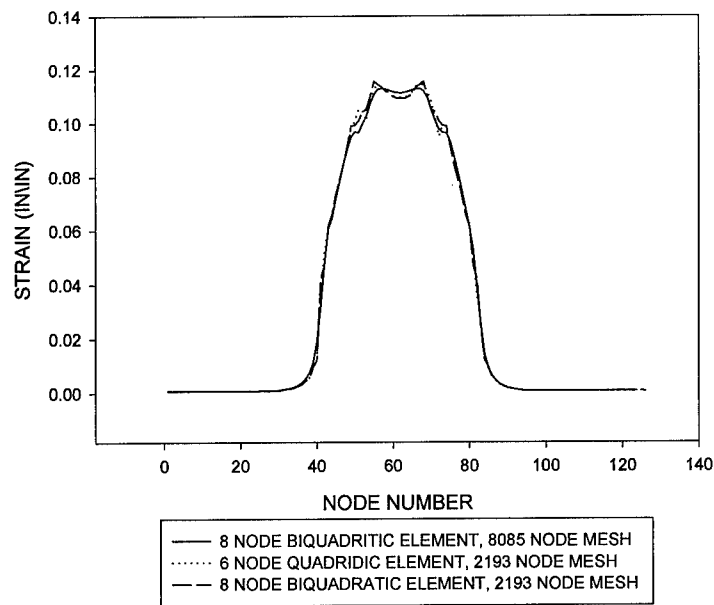
Figure 10: Strain Predicted by the Three Different Finite Element Models of
The Tapered Tensile Specimen along a Longitudinal Path
Corresponding to an Outside Edge of the Gage Section.

45
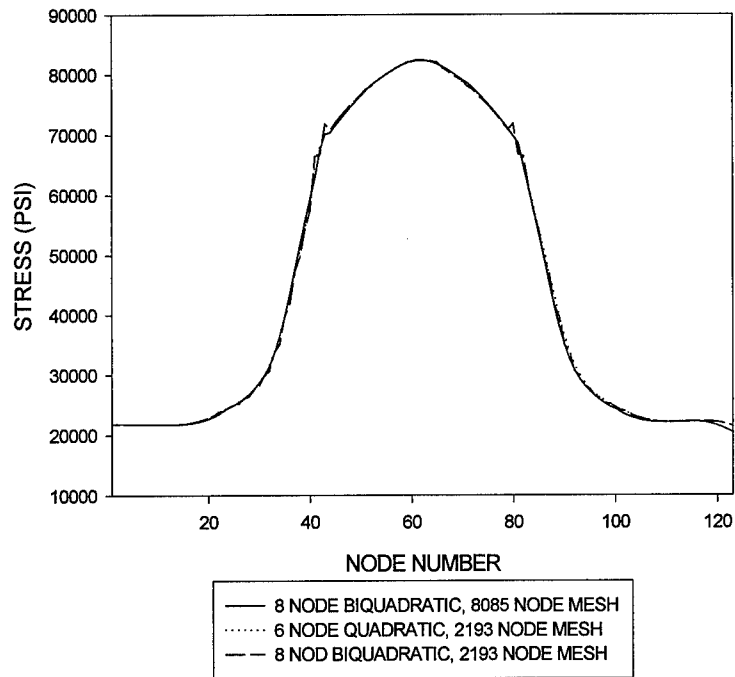
Figure 11: Stress Predicted by the Three Different Finite Element Models of the Tapered Tensile Specimen along the Longitudinal Centerline.
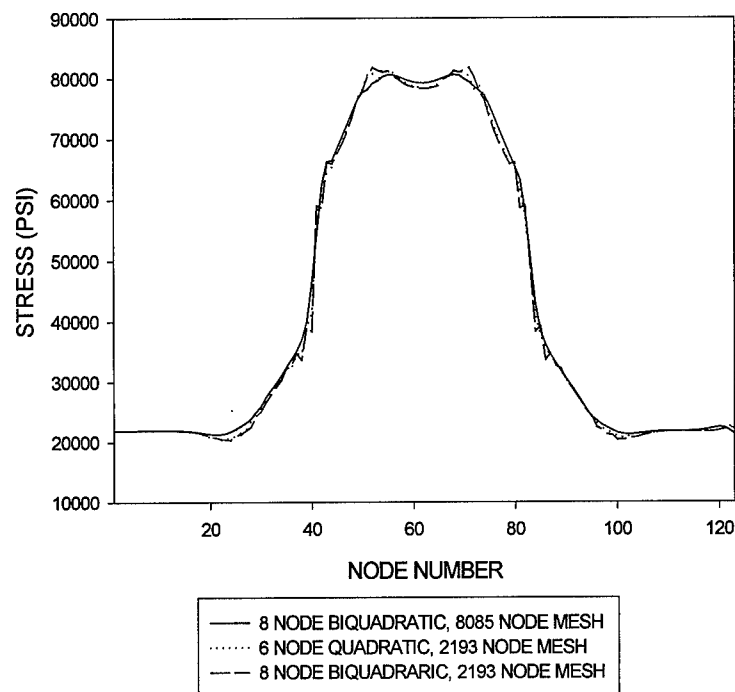
Figure 12: Stress Predicted by the Three Different Finite Element Models of the Tapered Tensile Specimen along a Longitudinal Path Corresponding to an Outside Edge.
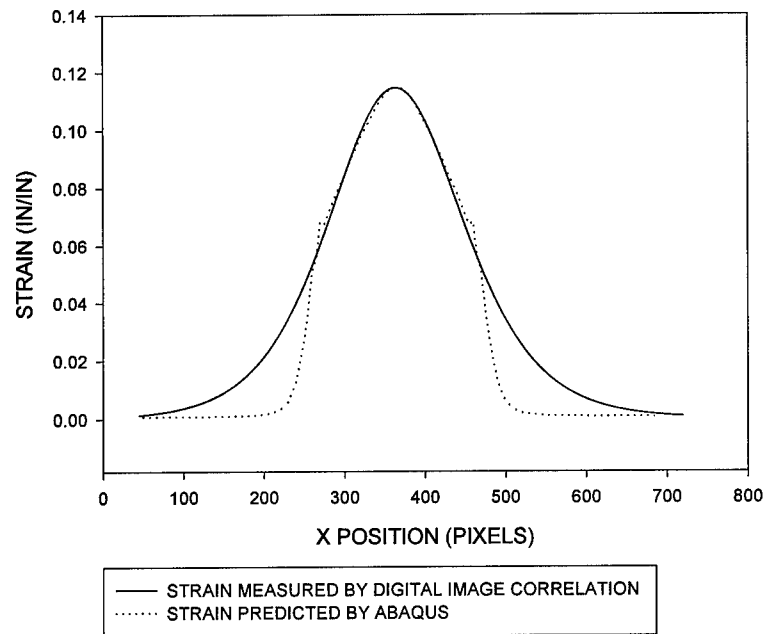
Figure 13: Strain Predicted by the Finite Element Model Compared to the Strain Measured by Digital Image Correlation along a Longitudinal Path Corresponding to the Centerline of the Specimen.
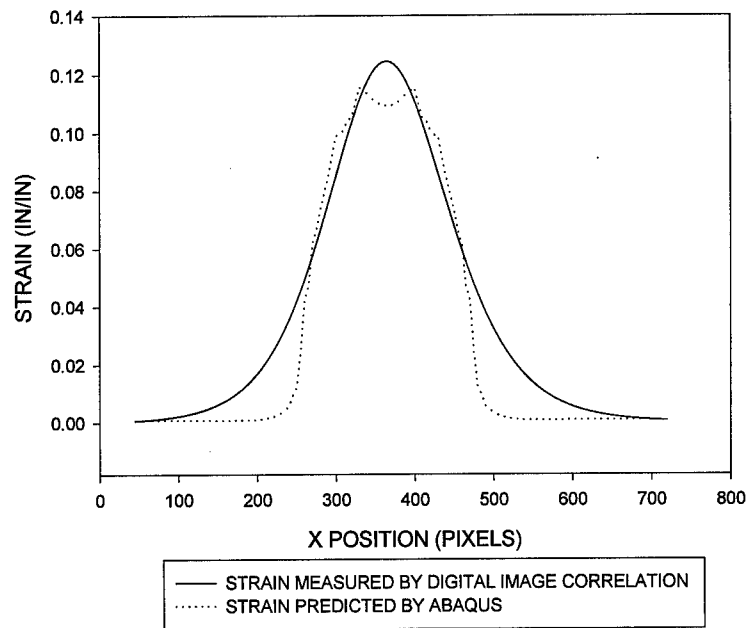
Figure 14: Strain Predicted by the Finite Element Model Compared to the Strain Measured by Digital Image Correlation along a Constant Longitudinal Path Corresponding to an Outside Edge of the Gage Section.
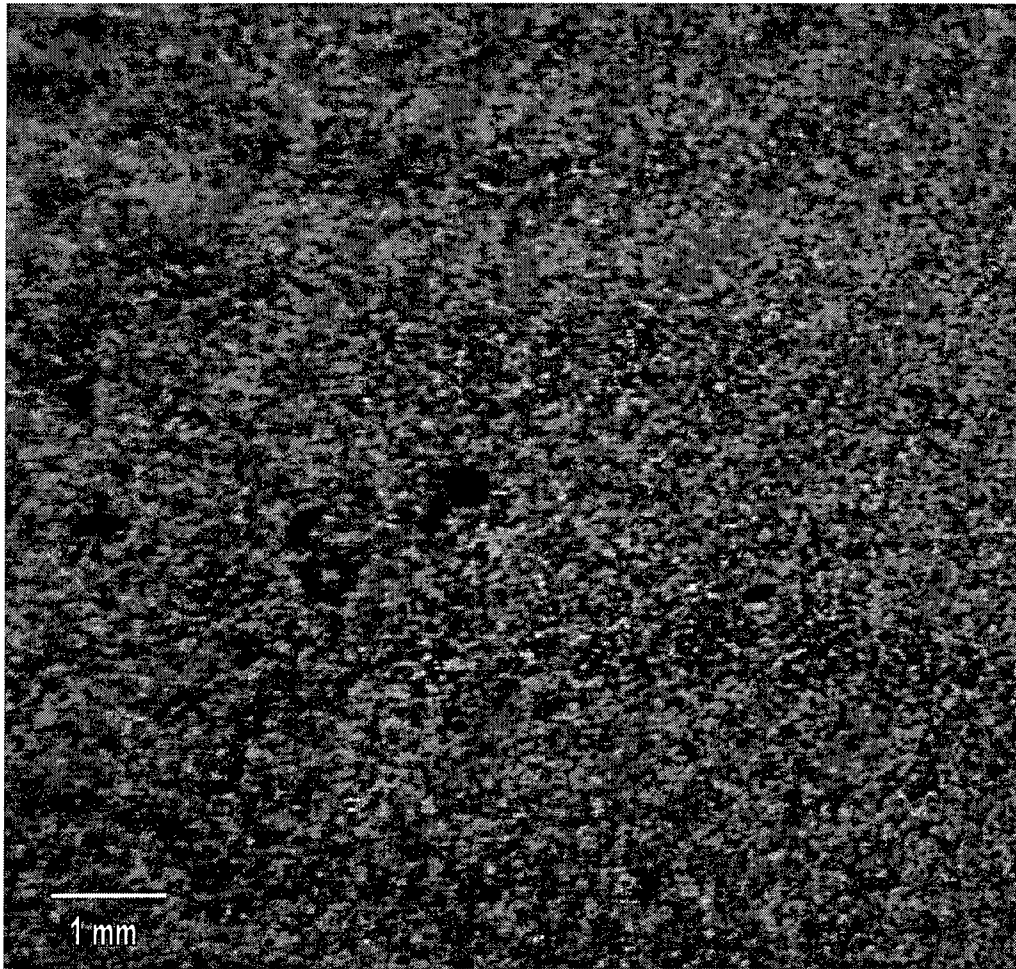
Figure 15: Image Showing Random Black and White Speckle Pattern and
.0135 Inch Diameter Hole
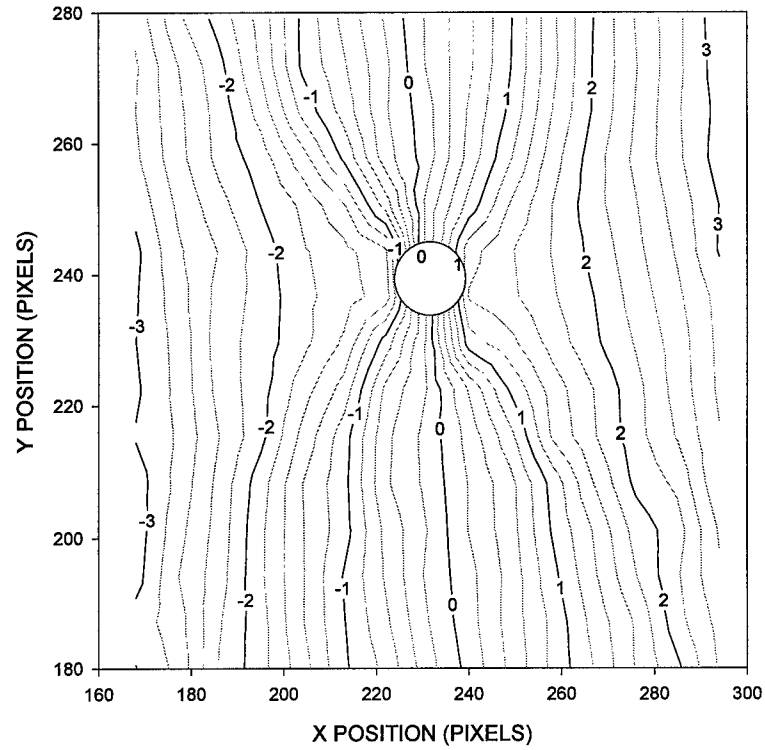
Figure 16: Displacement Contours for Aluminum Sample With .0135 Inch Diameter Hole.
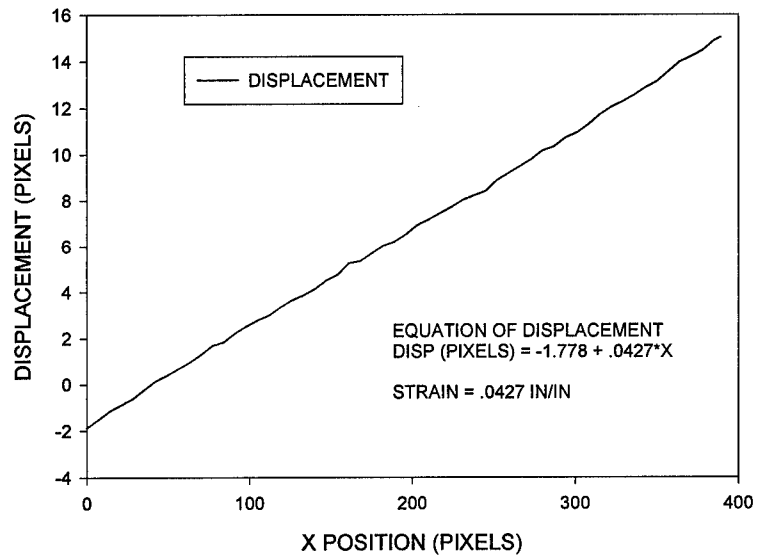
Figure 17: Displacement Curve For Aluminum Sample With .0135 Inch Diameter Hole Along the Edge Where the Extensometer was Attached.

49
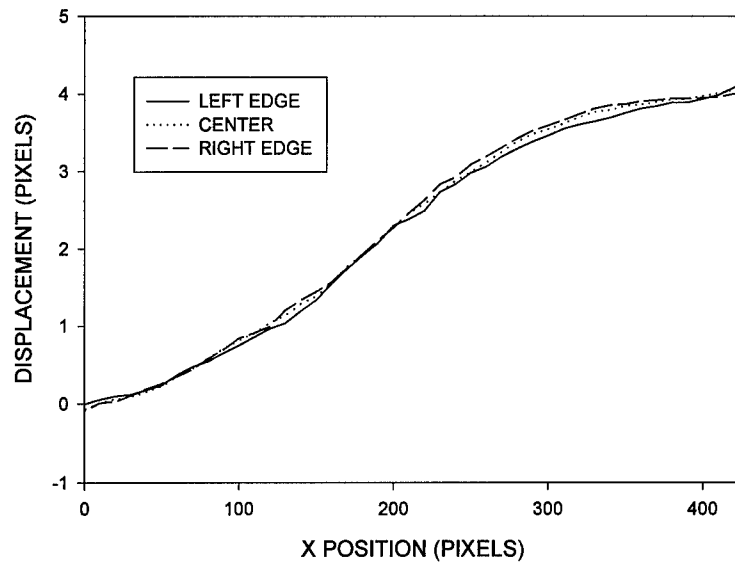
Figure 18: Displacement Versus X Position for the Top Surface of a Friction Stir Weld in 5454-O Aluminum along Three Constant Longitudinal Paths.
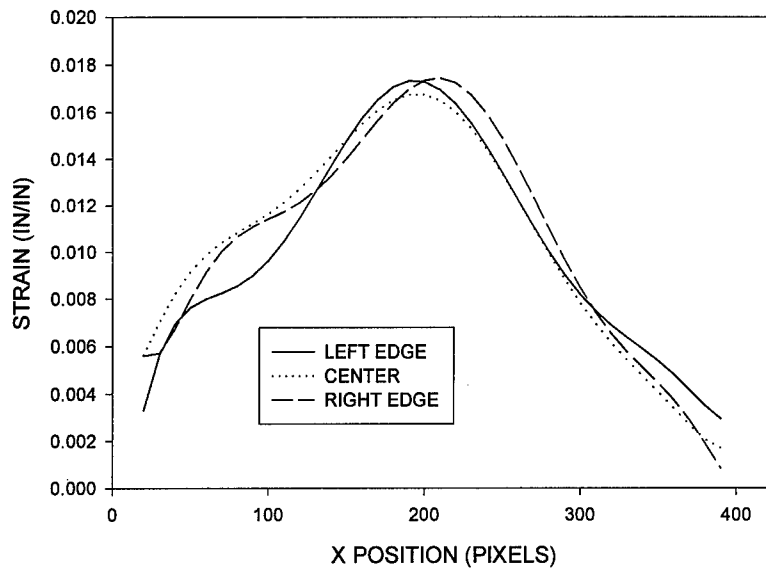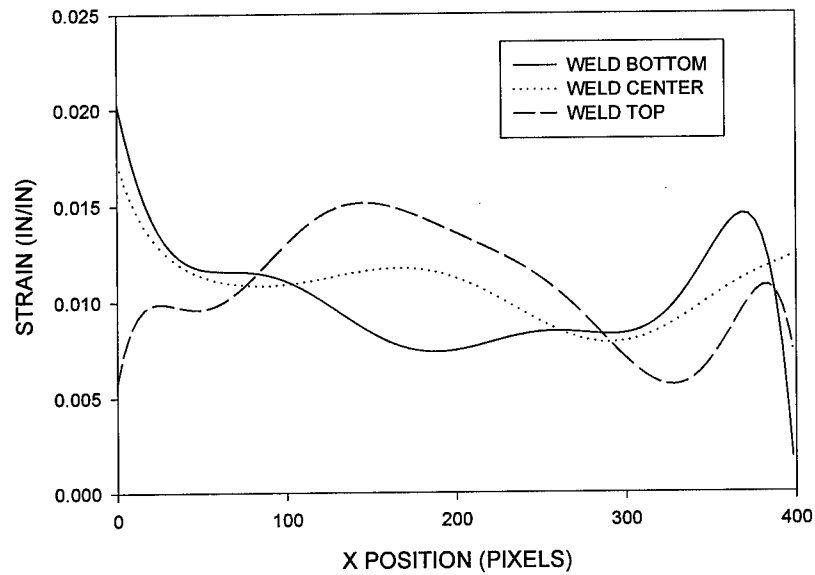

Figure 19: Strain Versus X Position for the Top Surface of a Friction Stir Weld in 5454-O Aluminum along Three Constant Longitudinal Paths. Strain Data is from the First Derivative of a Ninth Order Curve Fit to the Displacement Data in Figure 18.
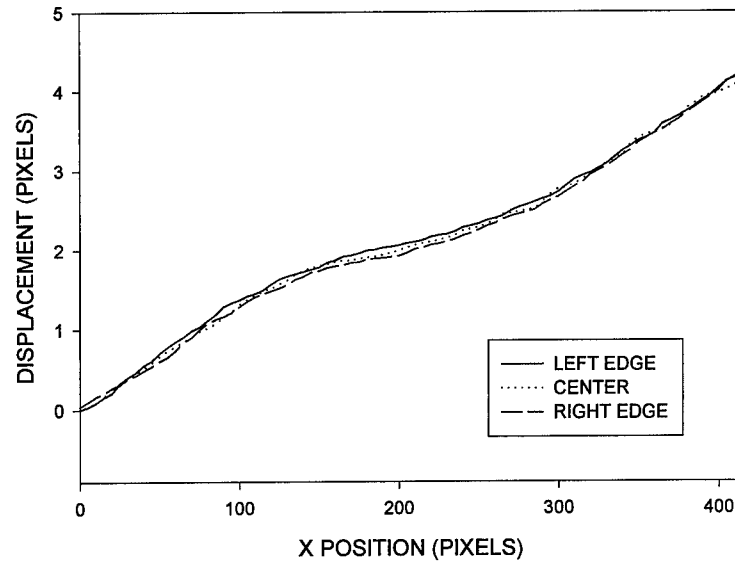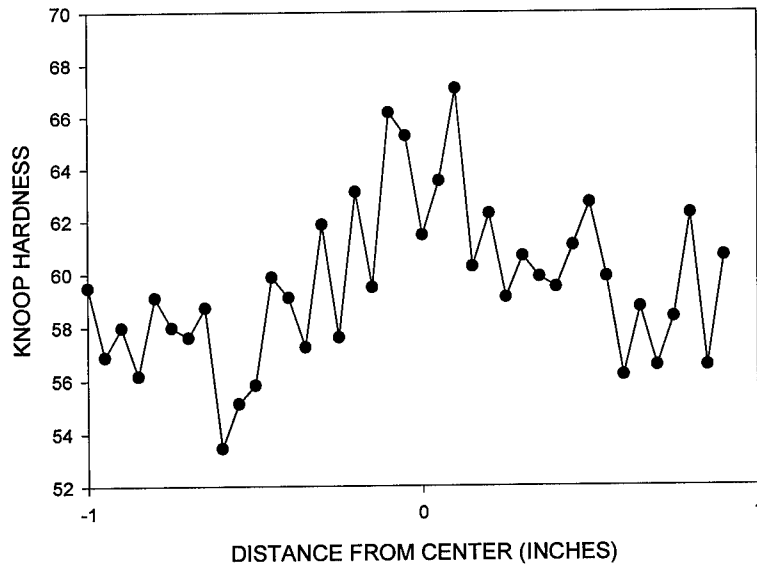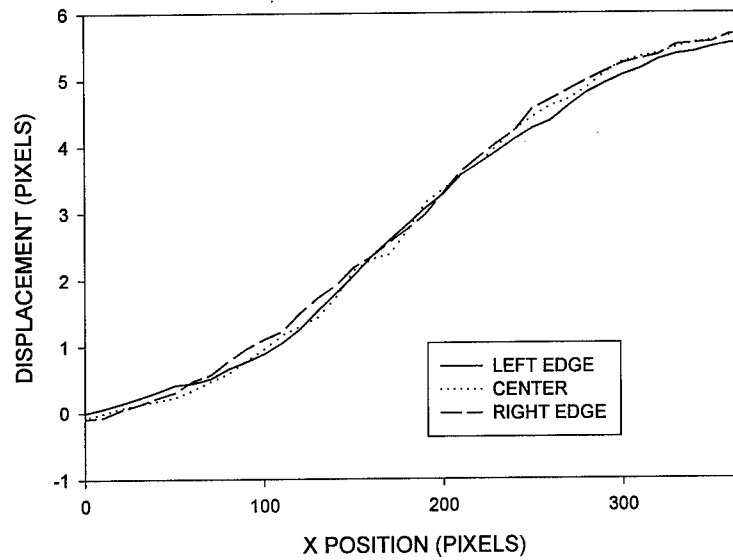
Figure 20: Displacement Versus X Position for the Back Surface of a Friction
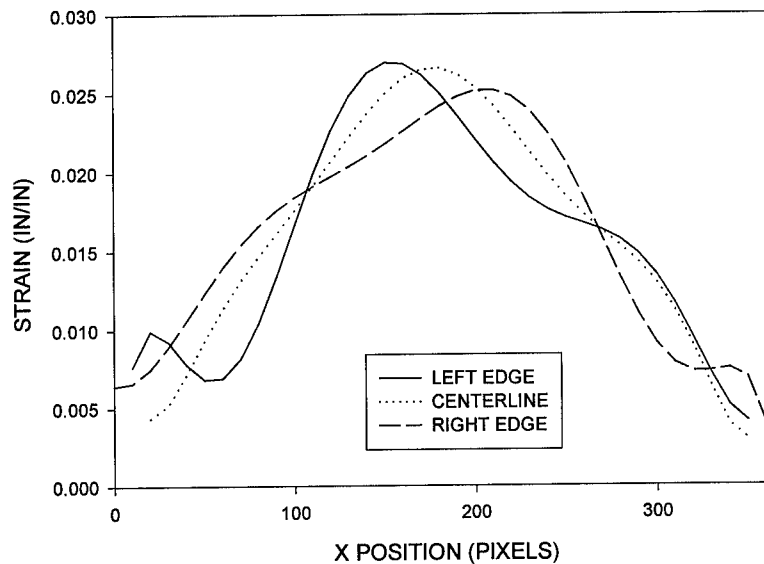Stir Weld in 5454-O Aluminum along Three Constant Longitudinal
Paths.
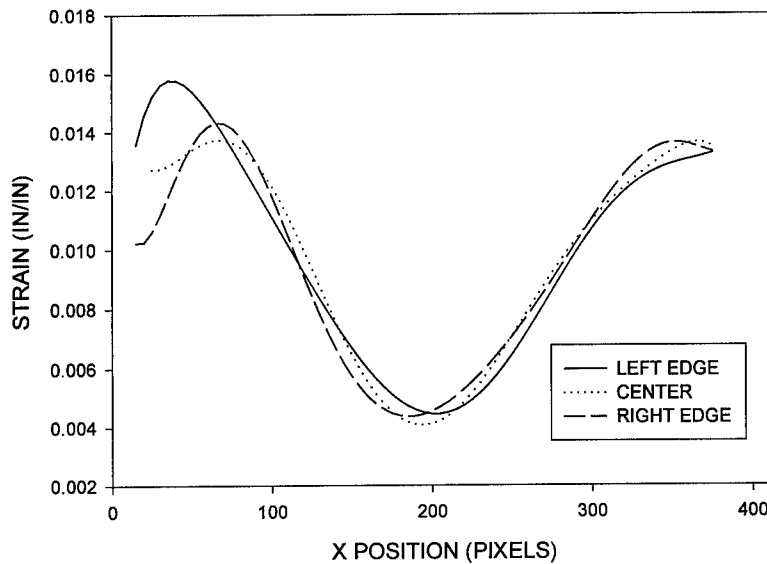
Figure 21: Strain Versus X Position for the Back Surface of a Friction Stir
Weld in 5454-O Aluminum along Three Constant Longitudinal
Paths. Strain Data is from the First Derivative of a Ninth Order
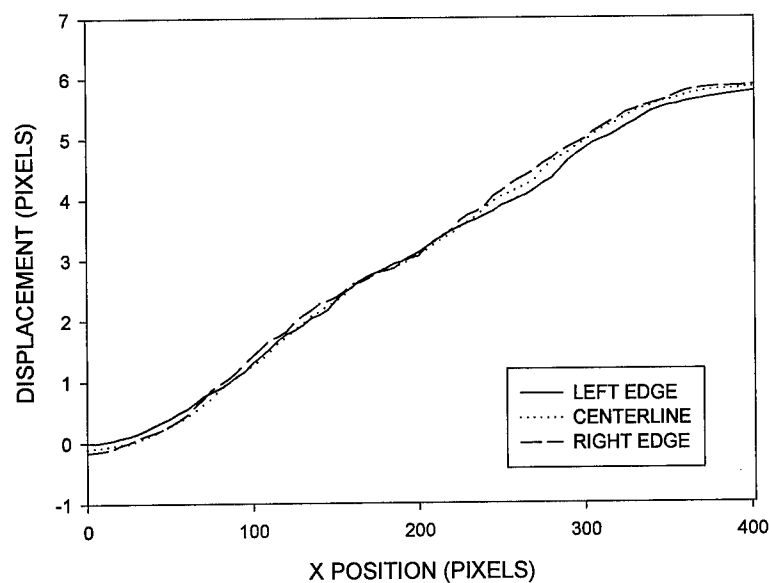Curve Fit to the Displacement Data in Figure 20.
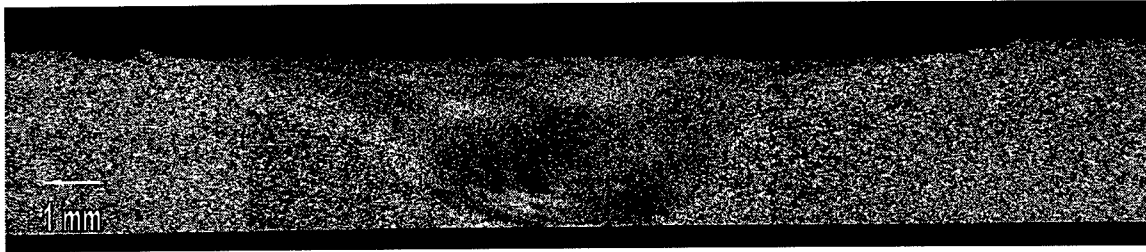
Figure 22: Etched Side Area of a Friction Stir Weld in 5454-O Aluminum. The Weld Nugget can be Seen in the Center with the Heat-Affected Zones on Either Side.
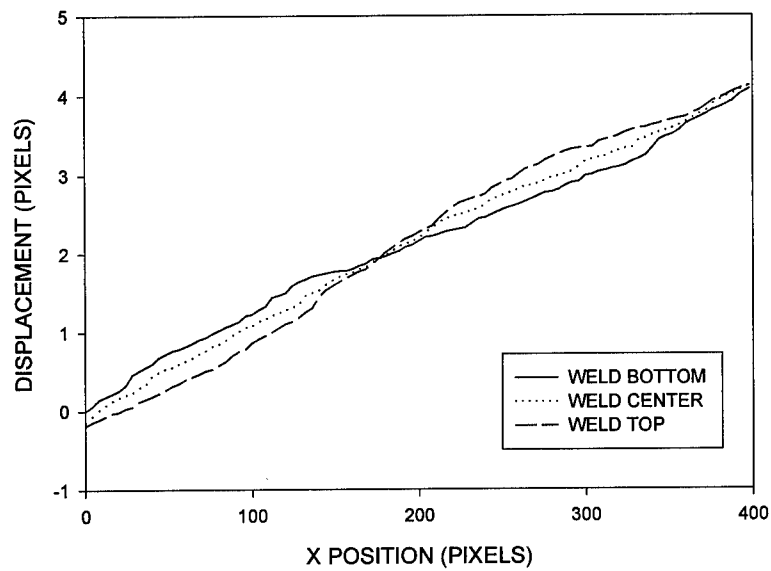
Figure 23: Displacement Versus X Position for the Side Surface of a Friction Stir Weld in 5454-O Aluminum along Three Constant Longitudinal Paths.
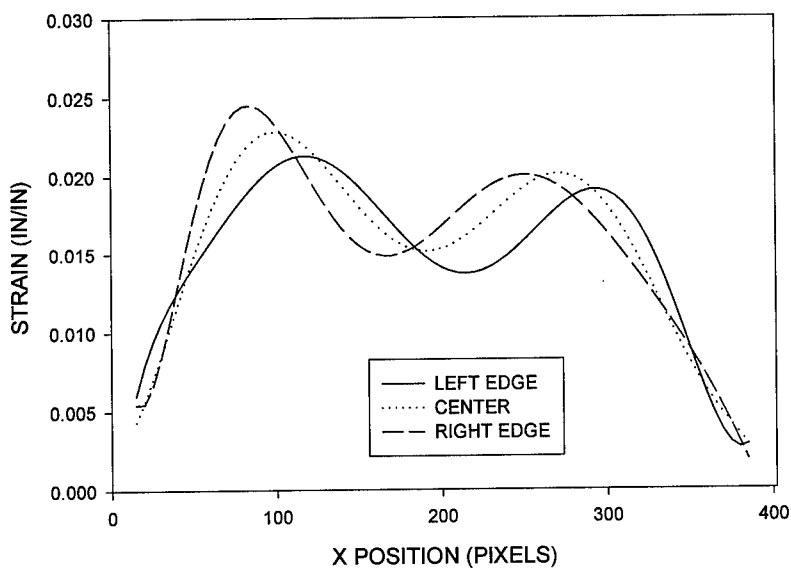
Figure 24: Strain Versus X Position for the Side Surface of a Friction
Stir Weld in 5454-O Aluminum along Three Constant Longitudinal
Paths. Strain Data is from the First Derivative of a Ninth Order
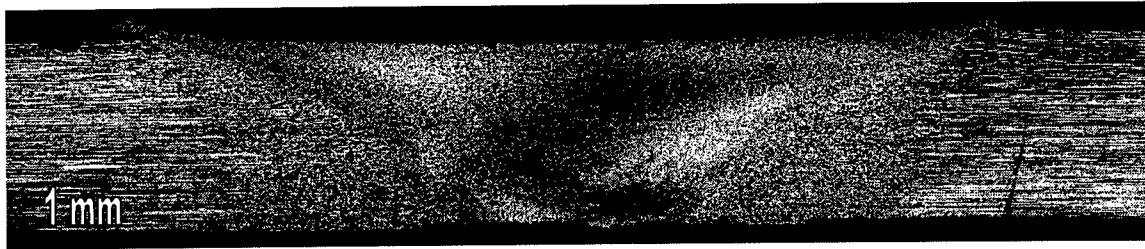Curve Fit to the Displacement Data in Figure 22.

Figure 25: Knoop Hardness Data for 5454-O Aluminum Friction Stir Weld.
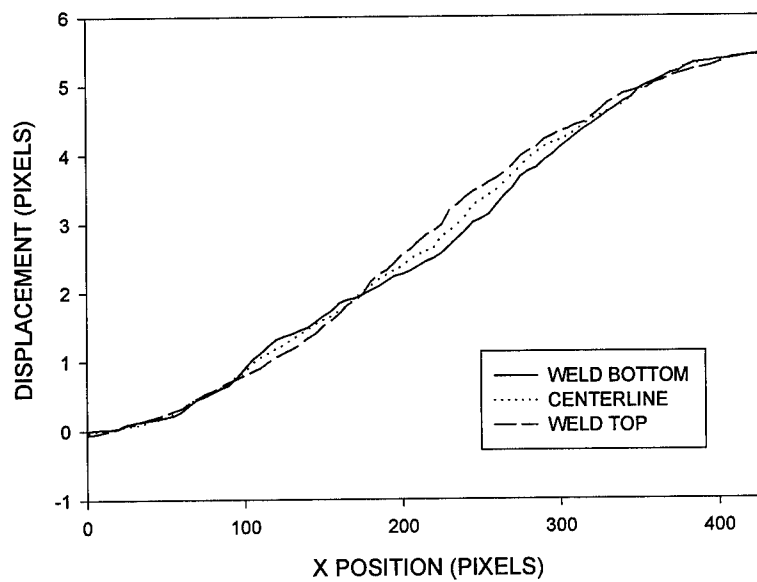Data Taken From the Side of the Weld Along its Longitudinal
Centerline.

Figure 26: Displacement Versus X Position for the Top Surface of a Friction Stir Weld in 5454-H32 Aluminum along Three Constant Longitudinal Paths.

Figure 27: Strain Versus X Position for the Top Surface of a Friction Stir Weld in 5454-H32 Aluminum along Three Constant Longitudinal Paths. Strain Data is from the First Derivative of a Ninth Order Curve Fit to the Displacement Data in Figure 26.

Figure 28: Displacement Versus X Position for the Back Surface of a Friction Stir Weld in 5454-H32 Aluminum along Three Constant Longitudinal Paths.
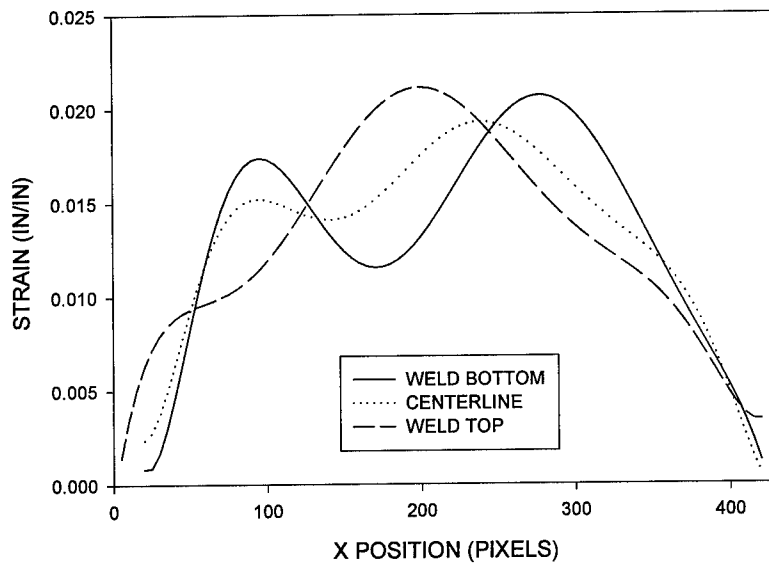

Figure 29: Strain Versus X Position for the Back Surface of a Friction Stir Weld in 5454-H32 Aluminum along Three Constant Longitudinal Paths. Strain Data is from the First Derivative of a Ninth Order Curve Fit to the Displacement Data in Figure 26.

Figure 30: Etched Side Area of a Friction Stir Weld in 5454-H32 Aluminum. The Weld Nugget can be Seen in the Center with the Heat-Affected Zones on Either Side.

Figure 31: Displacement Versus X Position for the Side Surface of a Friction Stir Weld in 5454-H32 Aluminum along Three Constant Longitudinal Paths.

56

Figure 32: Strain Versus X Position for the Side Surface of a Friction
Stir Weld in 5454-H32 Aluminum. Strain Data is from
the First Order Derivative of a Ninth Order Curve Fit to the
Displacement Data in Figure 28.
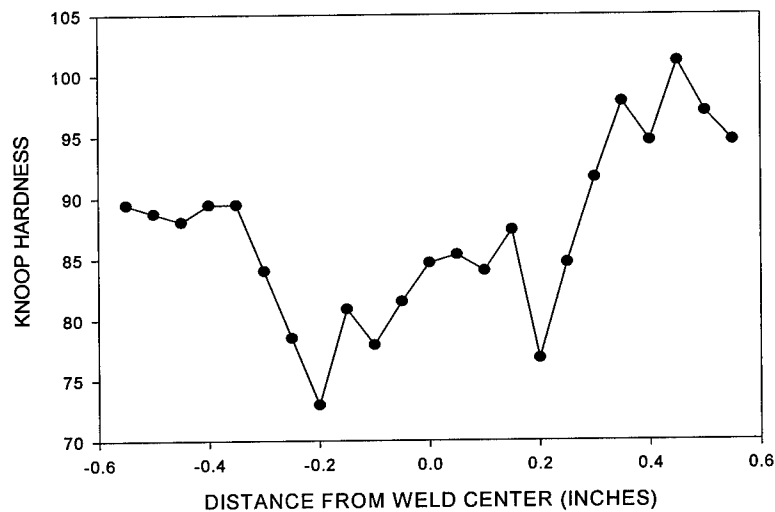
Figure 33: Knoop Hardness Data for 5454-H32 Aluminum Friction Stir Weld.
Data Taken From the Side of the Weld Along its Longitudinal
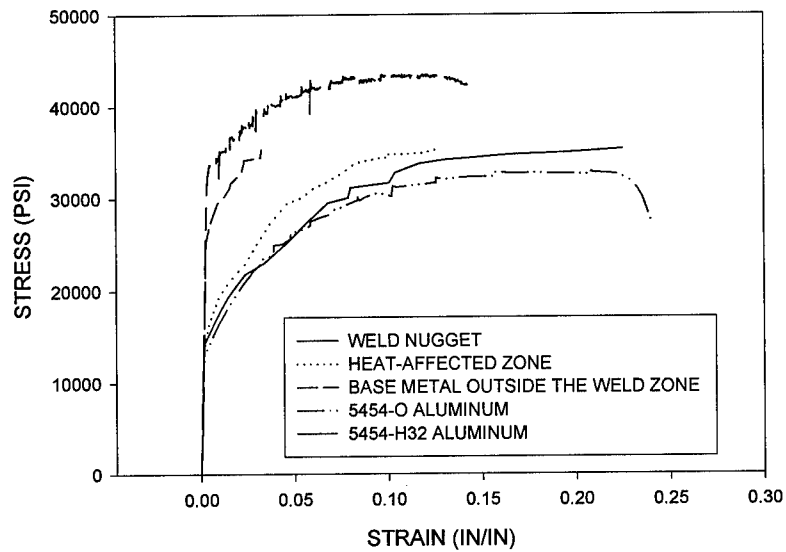Centerline.

Figure 34: Stress-Strain Curve for Weld Number 29 made with a Feed Rate of 3.4 Inches per Minute and a Spindle Speed of 270 rpm. Data taken along the Longitudinal Centerline.
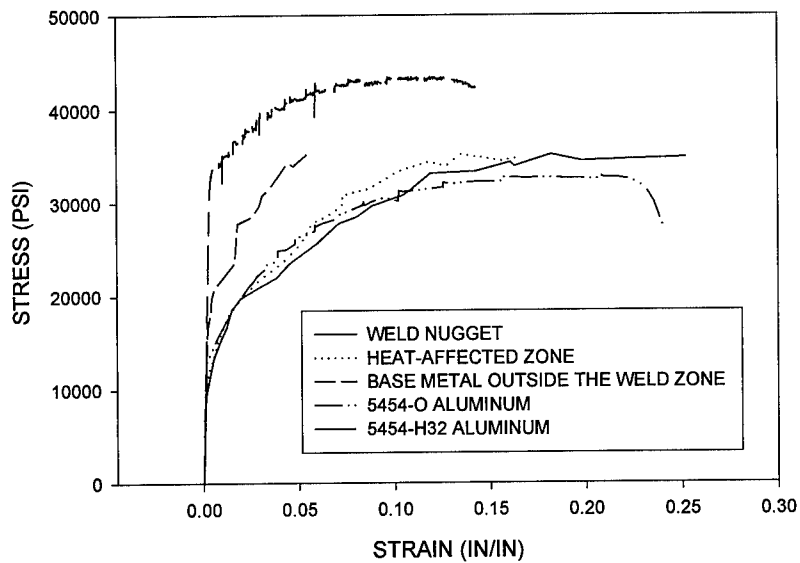

Figure 35: Stress-Strain Curve for Weld Number 30 made with a Feed Rate of 3.4 Inches per Minute and a Spindle Speed of 750 rpm. Data taken along the Longitudinal Centerline.
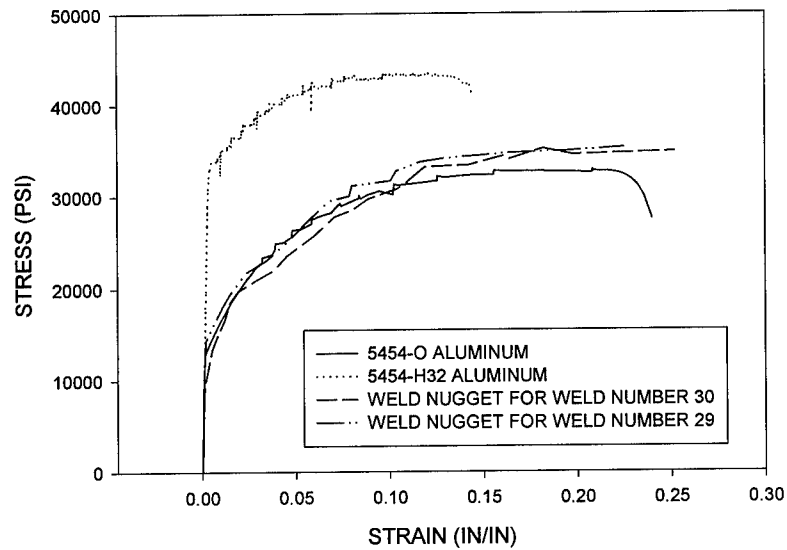
58

Figure 36: Stress-Strain Curve Comparing the Weld Nuggets for Welds 29 and 30 to the Stress-Strain Curves for 5454-O and 5454-H32 Aluminum. Data taken along the Longitudinal Centerline.
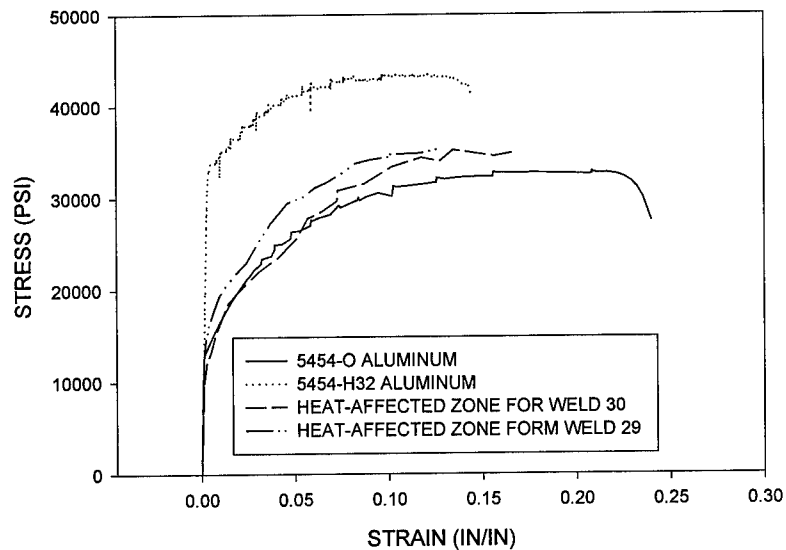

Figure 37: Stress-Strain Curve Comparing the Heat-Affected Zones for Welds 29 and 30 to the Stress-Strain Curves for 5454-O and 5454-H32 Aluminum. Data taken along the Longitudinal Centerline.
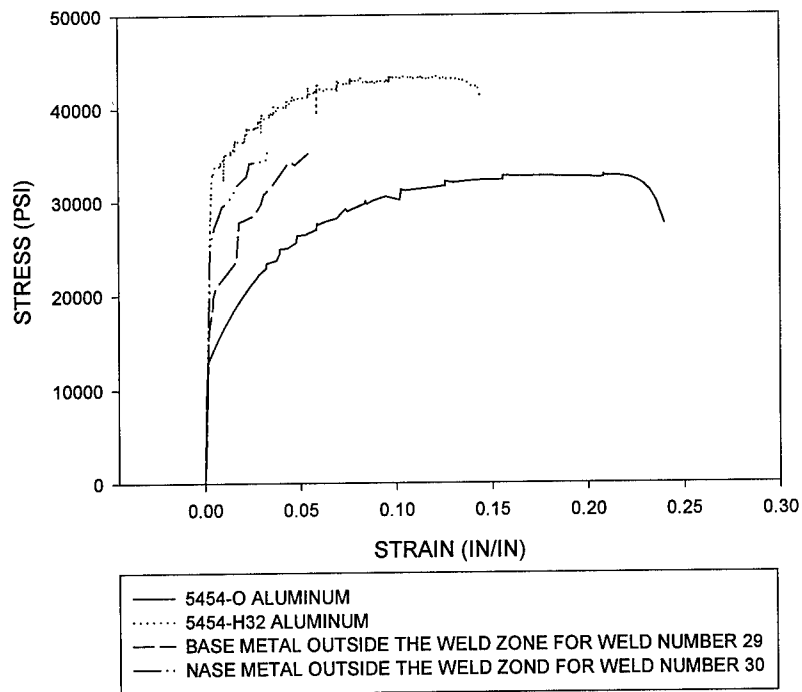
Figure 38: Stress-Strain Curve Comparing the Base Metal Outside of the Weld Zone for Welds 29 and 30 to the Stress-Strain Curves for 5454-O and 5454-H32 Aluminum. Data taken along the Longitudinal Centerline.
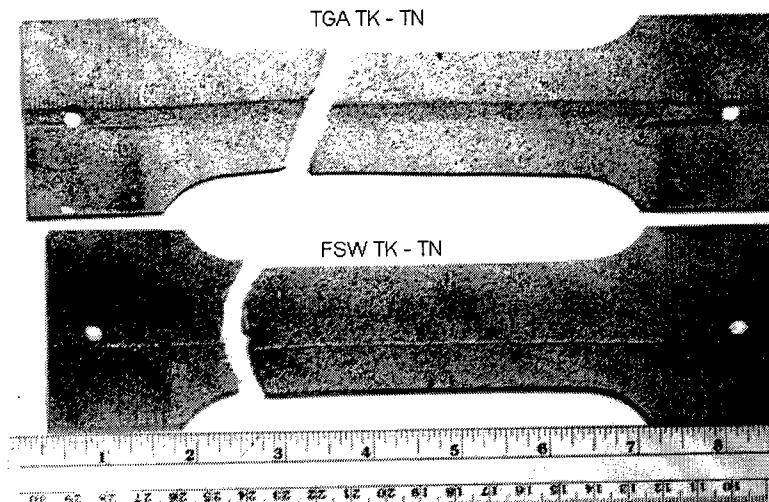

Figure 39: Image of Longitudinal Gas-Tungsten (TIG) and Friction Stir Weld.
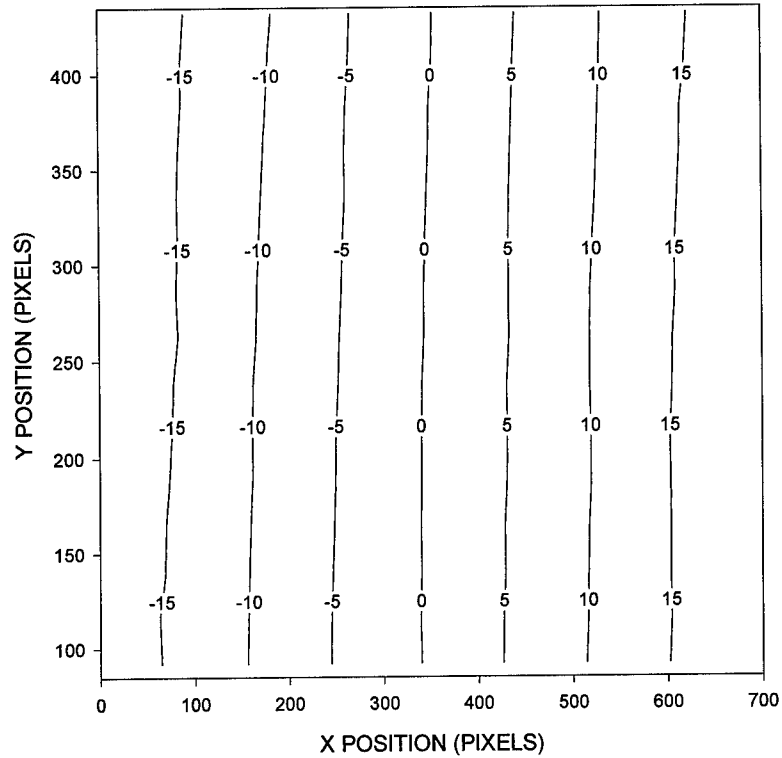
60

Figure 40: Surface Displacement Contours for the Top Surface of a Longitudinal
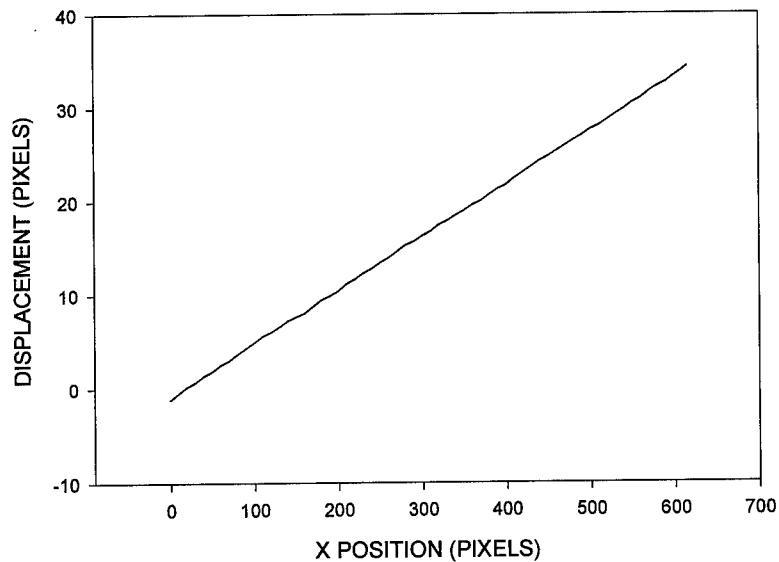TIG Weld Corresponding to 5.7% Strain.

Figure 41: Displacement along a Constant Y Path on the Surface of a TIG Weld
in 5454-O Aluminum. The Slope of the Displacement Data
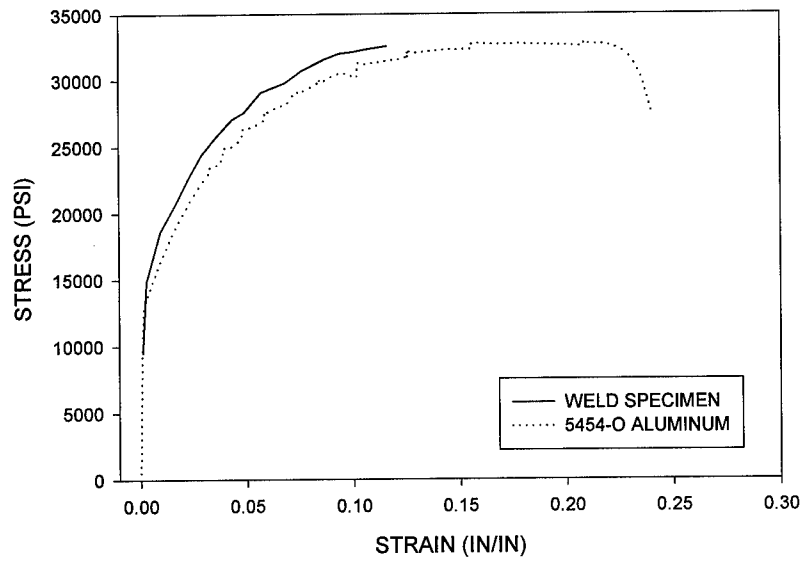Corresponds to 5.7% Strain.

61

Figure 42: Stress-Strain Data for a Longitudinal TIG Weld Plotted Along with the Stress-Strain Data for 5454-O Aluminum.

APPENDIX I

ABAQUS input file for 2193 node mesh using 8 node biquadratic elements.

```
*HEADING
Stainless Steel Tensile Specimen - 8 node biquadratic
*NODE
 1,0.,0.
 392,0.,1.2211
 460,.0295,1.3311
 732,.3305,1.8525
 902,.36,1.9625
 1242,.36,2.1425
 1412,.3305,2.2525
 1684,.0295,2.7739
 1752,0.,2.8839
 2177,0.,4.105
 17,.99,0.
 408,.99,1.2211
 476,.9605,1.3311
 748,.6595,1.8525
 918,.63,1.9625
 1258,.63,2.1425
 1428,.6595,2.2525
 1700,.9605,2.7739
 1768,.99,2.8839
 2193,.99,4.105
 4000,.0147,1.2761
 4001,.3453,1.9075
 4002,.3453,2.1975
 4003,.0147,2.8289
 4004,.9753,1.2761
 4005,.6447,1.9075
 4006,.6447,2.1975
 4007,.9753,2.8289
*NGEN,NSET=L1
 1,392,17
 460,732,17
 902,1242,17
 1412,1684,17
 1752,2177,17
*NGEN,LINE=P,NSET=L2
```

```
 392,460,17,4000
 732,902,17,4001
 1242,1412,17,4002
 1684,1752,17,4003
*NGEN,NSET=R1
 17,408,17
 476,748,17
 918,1258,17
 1428,1700,17
 1768,2193,17
*NGEN,LINE=P,NSET=R2
 408,476,17,4004
 748,918,17,4005
 1258,1428,17,4006
 1700,1768,17,4007
*NSET,NSET=LEFT
 L1,L2
*NSET,NSET=RIGHT
 R1,R2
*NSET,NSET=TOP,GENERATE
 2177,2193,1
*NFILL,NSET=TAPER
 LEFT,RIGHT,16
*ELEMENT,TYPE=CPS8
 1,1,3,37,35,2,20,36,18
*NSET,NSET=BOTTOM,GENERATE
 1,17,1
*ELGEN,ELSET=BODY
 1,8,2,1,64,34,8,1,0,0
*SOLID SECTION, ELSET=BODY,  MATERIAL=STAINLES
 .18
*MATERIAL, NAME=STAINLES
*ELASTIC
 27.6E6,.3
*PLASTIC
 29000.,0.
 36660.,.001034
 39130.,.00206
 40800.,.00306
 42060.,.004015
 43200.,.005096
 43860.,.006027
 44850.,.007111
 45300.,.008077
 46040.,.009077
 46600.,.01
 49400,.0152
```

```
 51460,.02
 53240,.025
 55180,.03
 56930,.035
 58570,.0401
 60040,.045
 61690,.05
 69300,.075
 76407,.1
 89500,.15
 142000,.3999
*BOUNDARY
 TOP,PINNED
*STEP,INC=5000000
*STATIC
 .01,50.,0.0001,1.
*BOUNDARY
 BOTTOM,2,,-.052
*EL PRINT,FREQUENCY=100
*NODE PRINT, FREQUENCY=100
*RESTART,WRITE,FREQUENCY=100
*END STEP
```

APPENDIX II

Diagram of the Finite Element mesh generated by the input file in Appendix I.